# Technology Readiness of 5th and 6th Generation Compliant Foil Bearing for 10 MWE S-$CO_2$ Turbomachinery Systems

**Hooshang Heshmat** **James F. Walton II*** **José Luis Córdova**

**Mohawk Innovative Technology, Inc.**
**1036 Watervliet-Shaker Rd,**
**Albany NY, 12205, USA**

**Dr. Hooshang Heshmat** is the lead Founder and President & CEO/Technical Director of Mohawk Innovative Technology, Inc. (MITI), an applied research and product development company specializing in advanced rotating machinery development. Since the inception of MITI in 1994, Dr. Heshmat has directed many new technological advancements specifically targeted toward advanced Oil-Free Rotating Machinery. Dr. Heshmat received his B.S. from The Pennsylvania State University in 1977 and his M.S. in 1979 and Ph.D. in 1988 in Mechanical Engineering from Rensselaer Polytechnic Institute (RPI). He is the Principal Investigator for a variety of programs concerned with applied tribology, including hydrodynamics, solid lubrication, and novel backup bearings for magnetically suspended rotor systems, tribochemistry and surface morphology.

**Mr. James F. Walton, II** is a Co-Founder and Vice President of Mohawk Innovative Technology, Inc. He received his B.S. in Mechanical Engineering from the University of Virginia, and his M.E. in Mechanical Engineering from the University of Florida. Mr. Walton, an ASME Fellow, has been involved in rotordynamics research and advanced product development for over 40 years. He has over 100 peer-reviewed technical publications in the areas of rotor bearing system dynamics, damping, foil bearings and powder lubrication. He has received numerous Best Paper Awards from engineering societies including ASME, AIAA, SAE and others and holds 5 U.S. patents.

**Dr. José Luis Córdova** is a senior scientist and program manager at MITI, in charge of analysis and design of turbomachinery and thermal management systems. He received his degree in Mechanical Electrical Engineering from the National Autonomous University of Mexico (UNAM), and both MS and PhD in Mechanical Engineering Science from the University of California at Berkeley (UCB). He has a broad background in mechanical engineering science that spans multiple fields, including combustion, fluid mechanics, heat transfer, thermodynamics, and applied engineering mathematics. At MITI, his contributions include the development of gas turbine engine recuperators, development of solid oxide fuel cell balance of plant technologies like blowers and heat exchangers, analysis of bearing coating tribochemistry, and other related fields.

*Corresponding Author: jwalton@mohawkinnovative.com

## ABSTRACT

The availability of bearings capable of sustaining long life and maintenance-free operation in the extreme temperature and pressure environments of supercritical carbon dioxide (s-$CO_2$) is key to the eventual commercial viability of s-$CO_2$ power generation systems. The development of advanced compliant foil bearings (CFBs) and tribological coatings capable of operation in such environments under high loads and speeds has been identified as key enabling technology for the development of s-$CO_2$ turbomachinery. Specifically, Korolon-coated 5$^{th}$ and 6$^{th}$ Generation (Gen 5 and Gen 6) oil-free CFBs have been demonstrated to operate at temperatures as high as 871$^{o}$C and journal/runner surface speeds as high as 550 m/sec. Without the speed and temperature limitations of conventional bearings, the aerodynamic and thermodynamic performance of turbomachinery improves significantly. Additionally, the use of foil bearings eliminates the need for liquid lubrication-support infrastructure, like oil delivery/scavenging pumps, cooling and oil-coking prevention mechanisms, filtration, and related maintenance, all of which add complexity to the system. It also eliminates the need for oil/gas seals to prevent the formation of unstable s-$CO_2$ and oil mixtures, which may result in hazardous byproducts such as carbonic acid and other carbonaceous materials. For all these reasons, the use of CFB-based s-$CO_2$ rotor/bearings system will result in essentially maintenance-free and long life turbomachinery.

Despite these clear advantages, CFBs have not yet gained universal acceptance due to two factors. The first is the perception based on old information that they are not yet robust enough for sustained performance in the demanding environments of s-$CO_2$ turbomachinery. The other one is that in contrast to the a-posteriori matching of other types of bearings to existing turbomachinery designs, the successful incorporation of CFBs into s-$CO_2$ turbomachinery requires an integral approach that treats the pairing as a single rotordynamic and thermal system, with all elements designed from inception for optimal interaction.

Thus, the objectives of this paper are twofold. First, we set out to offer an improved understanding of the rheological and tribological behavior of hydrodynamic CFBs operating in a supercritical fluid. Second, we present results of a tradeoff study and considerations for a recompression s-$CO_2$ closed cycle system that have led to the conceptual design configuration of a two-stage, 10 MWe ultra-high speed turbine powered generator. The turbine generator speed is deemed ultra-high since typical power generating systems are operated at least an order of magnitude lower speeds than the selected 55,000 to 60,000 rpm. This is twice the speed proposed for the GE 10 MWe s-CO2 turbine generator system and within 20% of the design speed for the DOE 250 kW supercritical carbon dioxide recompression closed Brayton cycle (RCBC) test assembly (TA) (Pasch, et al. 2014, Kalra, et al. 2014, Talbot, 2016). The interaction of the turbine with other system elements, like compressors, gear box and alternator and insight into the scalability of CFBs to systems between 1 to 100 MWe are also discussed. Based on the operating conditions identified in the tradeoff study, we also present a design for a test engine that will accommodate full-scale components and will operate with s-$CO_2$ as the process fluid at realistic speeds up to 60 krpm, pressures up to 20 MPa and temperatures up to 750°C. The test engine will generate relevant data for characterizing the rotordynamic and thermal performance of the CFB-supported test rotor and CFBs. We expect that this work will lay the foundation to ultimately demonstrate the immediate viability of Gen 5 and Gen 6 CFBs for enabling s-$CO_2$ power generation.

*Keywords:* Compliant Foil Bearings, CFBs, Gen 5, Gen 6, Oil-Free, 10 MW Power Generation, Supercritical Fluid, Carbon Dioxide, s-$CO_2$, Ultra-High Speed, Korolon

**TABLE OF CONTENTS**

## INTRODUCTION

The eventual commercial viability of supercritical carbon dioxide (s-$CO_2$) power generation and propulsion systems depends on the availability of bearings capable of sustaining long life and maintenance-free operation in the high rotational speeds and extreme temperature and pressure environments that characterize such systems. Typical turbine inlet conditions for s-$CO_2$ Brayton cycle systems present temperatures around 650°C and pressures in excess of 20 MPa (Fleming *et al*. 2013). Moreover, aerodynamic design theory dictates that the turbomachinery for these systems must operate at high rotational speeds—for example for 1 to 100 MW systems, rotor speed may range from 60,000 to 5400 rpm—and corresponding rotor weights may range from 100 to 18,000 kg.

Given the severe operating conditions of s-CO2 turbomachinery, traditional off-the-shelf bearing technology is not suitable for the high operating temperatures and in some cases speeds of these systems such as shown in the generalized schematic diagram of Figure 1. For example, rolling element bearings for aircraft gas turbine engine applications typically operate below 2.0 Million DN but often are limited in speeds at or below 1.5 MDN to achieve long life and require sophisticated lubrication systems and seals. At such high speeds, their operation results in high lubricant churning losses due to shear and restricted oil flow into and out of the bearing due to windage. Additionally, lubricants require cooling to prevent degradation or oil coking, and require seals to prevent process fluid contamination or chemical reaction. On the other hand, magnetic bearings, while overcoming the limitations of oil-lubricated bearings, add complexity and power loss due to required power electronics, sensors and controls. Magnetic bearings also suffer from poor response to high frequency/transient events and require back-up bearings, which increase weight, volume, cost and potential reliability issues with the myriad of sensors and electronic elements needed. Finally, temperature limitations for stator windings and magnetic materials would make operation above 300°C unlikely without substantial hardware and capital investments.

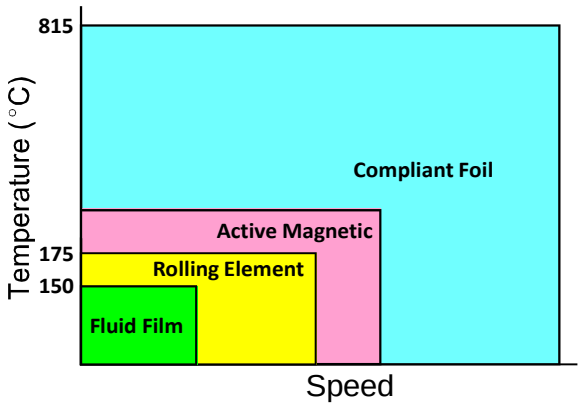


**Figure 1. Speed/Temperature capability of different bearing families**

For all these reasons, the development of advanced compliant foil bearings (CFBs) capable of optimal operation in such environments under high loads and speeds are a key enabling technology for the development of s-$CO_2$ turbomachinery. The use of oil-free CFBs eliminates speed and temperature limitations imposed by conventional bearings, and hence improves turbomachinery performance. It also eliminates the need for liquid lubrication-support infrastructure, like oil delivery/scavenging pumps, cooling and oil-coking prevention mechanisms, filtration, and related maintenance, all of which add complexity to the system. It also eliminates the need for oil/gas seals to prevent the formation of unstable s-$CO_2$ and oil mixtures, which may result in hazardous byproducts such as carbonic acid and other carbonaceous materials. This reduction of complexity resulting from the use of CFB-based s-$CO_2$ rotor/bearings system ultimately translates into essentially maintenance-free and long-life turbomachinery

Despite all these clear advantages, CFBs have not yet gained universal acceptance due to two factors: perception and inexperience in foil bearing design and system integration. The first factor is the perception that foil bearings are only suitable for small lightweight and high-speed rotors. The perception

of foil bearings applying only to small rotors relies on limited information about advances being made in the technology or a prior negative experience with foil bearings. The authors have personally encountered other researchers or system developers who indicate they do not consider foil bearings robust enough for sustained performance in the demanding environments (particularly the high loads and temperatures) due to a prior experience or hearsay from failed applications from twenty years ago. In a report on Multi-Megawatt s-$CO_2$ turbomachinery (Fleming et al. 2013), limited experience with low capacity foil bearings resulted in a recommendation to use oil-lubricated tilt pad bearings. Yet there exists a wealth of data indicating otherwise. For example, DellaCorte and Valco report (2000) reported Foil Bearing Generation classifications (2000) based on Heshmat's experimental method for determining foil bearing load capacity (1982, 1993, 1994). Subsequently, Heshmat and others have reported on advancements that identify capabilities above and beyond DellaCorte's load carrying capacity assessment (Heshmat et al., 2004-2018, Jahanmir et al., 2009, Heshmat 2005; See Figure 2).

| Class | Load Capacity (PSI/MPa) | Stiffness | Damping | Speed Limit | Shock Tolerant | Size (mm) | Misalign Capable | ≤ 175°C | ≤ 370°C | ≤ 480°C | ≥ 650°C | ≥ 815°C |
|---|---|---|---|---|---|---|---|---|---|---|---|---|
| I | 15/.103 | Low | Very Low | Low | No | 30-50 | Very Low | ✔ | | | | |
| IIA | 33 /.23 | Low | Low | Med | No | 30-50 | Low | ✔ | | | | |
| IIB | 50 /.35 | Med | Low | M-H | Med | 25-75 | Low-Med | ✔ | ✔ | | | |
| III[1] | 100/.69 | Med | Med | High | Yes | 15-100 | Med | ✔ | ✔ | | | |
| IV[2-4] | 100/.69 | High | High | Unlim | Yes | 6-240 | Med-High | ✔ | ✔ | ✔ | | |
| V[5] | 100/.69 | 3-D | High+ | Unlim | Yes | 6-240 | High | ✔ | ✔ | ✔ | ✔ | |
| VI[6] | 100/.69 | 3-D | High+ | Unlim | Yes | 6-240 | High | ✔ | ✔ | ✔ | ✔ | ✔ |

1.DellaCorte (2000), 2-4.Heshmat (2005), (2006), (2004), 5.Salehi (2007), 6.Heshmat (2018)

**Figure 2. Capabilities of advanced Generation foil bearings**

The second factor influencing application of foil bearings relates to knowledge and experience in designing systems applying foil bearings. In contrast to traditional bearings, the successful incorporation of CFBs into s-$CO_2$ turbomachinery requires an integrated approach that treats the pairing as a single rotordynamic and thermal system, with all elements designed from inception for optimal interaction, and it is unlikely that advanced CFBs can serve in existing turbomachinery as drop-in replacements for traditional bearings

Thus, the *first objective* of this paper is to re-visit the physics governing CFB behavior, and through comparing and contrasting our analysis to previously published work (Dousti & Allaire, 2016) to offer an

improved understanding of the physics governing the rheological and tribological behavior of hydrodynamic CFBs operating in s-$CO_2$. By use of numerical computations presented here, we attempt to dispel any misconceptions that put into question the superior load capacity and stability characteristics of $5^{th}$ and $6^{th}$ generation (Gen V and Gen VI) foil bearings for s-$CO_2$ applications (per Figure 2).

The *second objective* of this paper is to present results of a tradeoff study performed as well as considerations required to design of a CFB-supported two-stage power turbine for a net 10 MWe output recompression s-$CO_2$ cycle system. The following sections present operating and thermodynamic cycle conditions along with explanations of how these affect and define the system layout, the turbine type as well as its interaction with other system elements, such as compressor, gearbox, and alternator. As part of this second objective, we also address the scalability and applicability of the CFB technology to a broader range of power generation requirements. Currently a target capacity of 10 MWe is considered ideal for concentrated solar energy systems, waste heat recovery, or commercial bottoming and auxiliary system applications. However, space and military applications may benefit from the availability of lower capacity systems, say 1 to 5 MWe, while the eventual replacement of fossil fuel-based power plants would likely explore s-$CO_2$ options in the tens to hundreds of megawatts, say 100 to 300 MWe.

Finally, we present a design for a dynamic test system to characterize the rotordynamic and thermal performance of Gen V and Gen VI CFBs that will accommodate full-scale components, and will operate using s-$CO_2$ at conditions identified as optimal by the aerodynamic analysis for the 10 MWe power turbine design presented. At 55,000 to 60,000 rpm, these optimal but very high-speed conditions can only be achieved via and oil-free scheme, i.e. a CFB-supported system. The test system will be designed to operate at pressures up to 20 MPa and temperatures up to 750°C.

We expect that this work will lay the foundation to ultimately demonstrate the immediate viability of Gen V and Gen 6 CFBs as an enabling technology for s-$CO_2$ power generation. Additionally, we expect the results will benefit both the scientific and engineering communities by contributing to the understanding of methods and resources needed to develop efficient and reliable turbomachinery for s-$CO_2$ power conversion systems.

## CFBS IN SUPERCRITICAL FLUID

According to lubrication theory, there are two regimes for hydrodynamic bearing operation: incompressible and compressible. Figure 3 shows a qualitative relationship between a bearing's load capacity and the speed (or more generally the Reynolds number) at which it is operating. In the figure, rolling element bearings are seen as the boundary of the blue region to have a constant load capacity over a range of speeds, but drop dramatically once a certain critical speed is passed. Rigid fluid bearings, shown by the red curve, have a load capacity that increases with speed, reaches a maximum, and abruptly collapses after a certain speed value is exceeded. Only compliant foil bearings, shown by the blue curve exhibit a monotonically increasing load capacity over a range of speeds, even as they transition from the incompressible to the compressible bearing regime. Figure 4 shows that in particular, $CO_2$ sustains a compressible bearing operation regime even at pressures as high as 15 MPa and temperatures to 650°C, where use is made of the hydrodynamic lubrication bearing number definition, $\Lambda = (6\mu\omega/p_a)(R/C)^2$, to identify the compressible (i.e., $\Lambda \gtrsim 0.05$) and incompressible lubrication regions (i.e., $\Lambda \lesssim 0.05$).

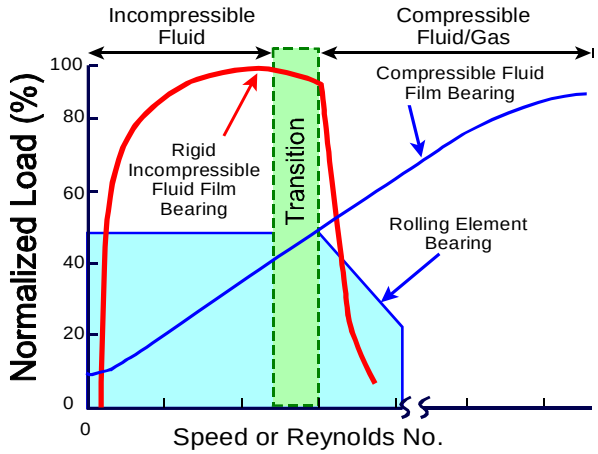


**Figure 3. Bearing technology load vs speed**

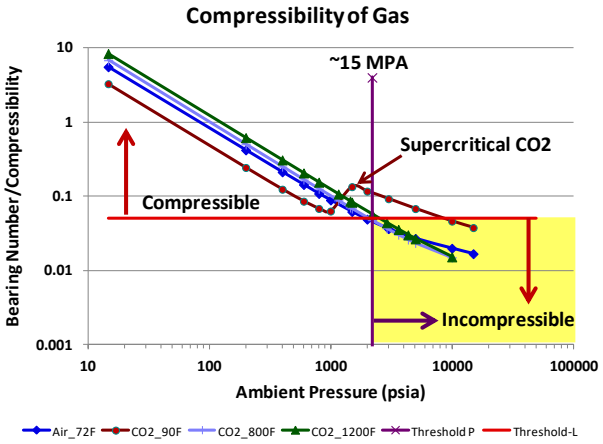


**Figure 4. $CO_2$ compressible/incompressible regimes**

## Incompressible Bearing Behavior

This discussion begins with incompressible fluid film bearings. While capable of supporting very large loads, incompressible rigid pad hydrodynamic bearings suffer from the limitation that turbulence in the fluid film at high Reynolds numbers increases power losses and bearing load capacity drops due to a substantial increase in temperature.

To properly assess and design rigid hydrodynamic bearings, it is important to take into account the governing equations and boundary conditions. In this case, the pressure and temperature distributions ($P(\theta,z)$ and $T'(\theta,z)$) are governed by two coupled linear differential equations, namely, the Reynolds equation [1] and the energy equation [2]. The incompressible Reynolds equation is as follows:

$$\frac{1}{R}\frac{\partial}{\partial\theta}\left[G_x\frac{h^3}{\mu' R}\frac{\partial p}{\partial\theta}\right]+\frac{\partial}{\partial z}\left[G_z\frac{h^3}{\mu'}\frac{\partial p}{\partial z}\right]=6\omega\frac{\partial h}{\partial\theta}+12\frac{\partial h}{\partial t} \tag{1}$$

Here, $\mu'$ is the local fluid dynamic viscosity which may be a function of the local temperature T' and G accounts for turbulence and density variations. The two-dimensional energy equation is obtained through integration across the film thickness to yield:

$$\rho ch\left(6\omega R-G_x\frac{h^2}{\mu' R}\frac{\partial P}{\partial\theta}\right)\frac{1}{R}\frac{\partial T'}{\partial\theta}-\rho cG_z\frac{h^3}{\mu'}\frac{\partial P}{\partial z}\frac{\partial T'}{\partial z}=\frac{12\mu'\omega^2R^2}{hG_\tau}+\frac{h^3}{\mu'}\left\{\frac{G_x}{R^2}\left(\frac{\partial P}{\partial\theta}\right)^2+G_z\left(\frac{\partial P}{\partial z}\right)^2\right\} \tag{2}$$

Here, the left hand side of the equation (2) represents convection of energy away from the point in the film; the first term on the right represents rotational shear induced energy dissipation; and the second right hand term represents energy dissipation due to pressure gradients. In all cases, the continuity equation is satisfied (conservation of mass).

In order to properly characterize bearing performance both the Reynolds and energy equations have to be solved simultaneously, including local variations in the fluid density, viscosity and laminar/turbulence conditions in an iterative manner to determine start of the film, $\theta_1$, minimum film, $\theta_0$, and end of film, $\theta_2$, defined in the schematic shown in Figure 5 (Heshmat, 1988). The iterative approach is necessary since the pressures, film height and start and end of the film are unknown a priori. Clearly, such a solution will be dependent upon the assumed boundary and initial conditions.

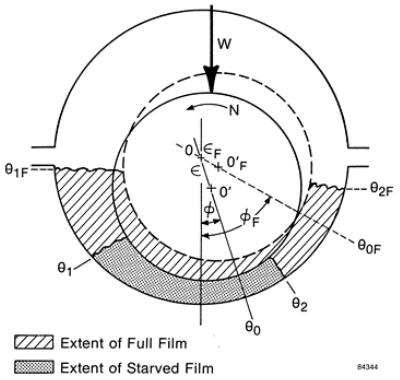


**Figure 5. Fluid film bearing coordinate system**

For example, it was noted in Dousti & Allaire (2016) that the predicted pressure profile in the diverging region of the bearing resulted in bearing pressures well below the ambient boundary condition of 8 MPa to a minimum value of less than 5 MPa, as shown in Figure 6. In their paper, Dousti & Allaire (2016) have used Reynolds' incompressible fluid film equation (1886) for an infinitely long bearing, which will predict negative pressures but which will incorrectly predict bearing sub-ambient pressures and hence affect bearing load. Sommerfeld (1904) provided a reasonable approximation at the trailing end of the pressure curve to overcome the incorrect sub-ambient pressure predictions resulting from the Reynolds boundary conditions, known as Sommerfeld substitutions (Pinkus & Sternlicht 1961). The trailing boundary conditions are treated by setting the negative pressure regions to zero. Numerous other papers confirm the validity of using variations on Sommerfeld's substitutions, and in fact provide an enhancement, in which both the pressure and the gradient are set to zero wherever the gradient goes negative, i.e., $p(\theta_2) = 0$ and $\partial P/\partial\theta|_{\theta 2} = 0$, where $\theta_2$ is the location where the pressure goes negative (Pinkus & Sternlicht 1961,Heshmat 1984, 1988, 1991). In fact, as shown in Figure 7, it was previously demonstrated that the bearing minimum pressure cannot be lower than the ambient pressure (Heshmat, 1988). Here film pressures in the diverging regions of the bearing revert to the ambient boundary pressure condition (i.e., $\theta_2$ >220°). Thus, it would seem that film pressure profile with trailing edge sub ambient pressures shown in Figure 6 are in conflict with theory and experiment.

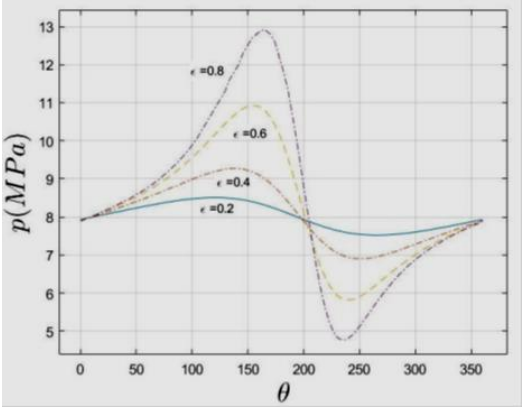


**Figure 6. Centerline pressure profiles at various eccentricities from Dousti & Allaire (2016)**

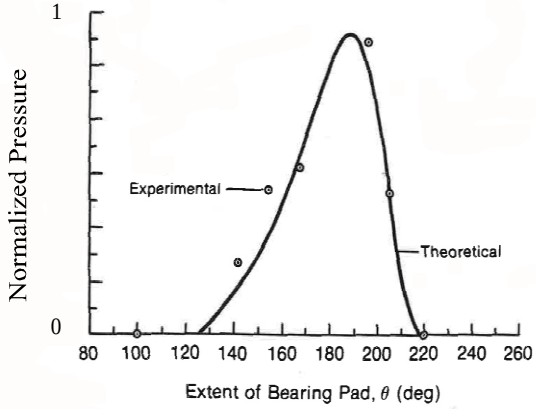


**Figure 7. Experimental and theoretical bearing pressure from Heshmat (1988)**

Another issue arising from their solution was found when analyzing the s-$CO_2$ properties for the given pressure and density in their hydrodynamic bearing. Figure 8 shows the density and pressure data from Figure 6 overlaid with the corresponding temperatures calculated by use of REFPROP. Figure 9 shows the same state data recast on a T-s diagram, also calculated via REFPROP. As can be seen, their calculations appear to indicate that as the fluid expands, the temperature rises. This is incongruent with the Second Law of Thermodynamics. This seems to reinforce that the pressures predicted by their model are incorrect.

Given these differences and incongruities, it appears that the assumptions and boundary conditions used by Dousti & Allaire will lead to erroneous conclusions regarding rigid pad bearing performance with s-$CO_2$. The total load carrying capacity of the bearing determined from the

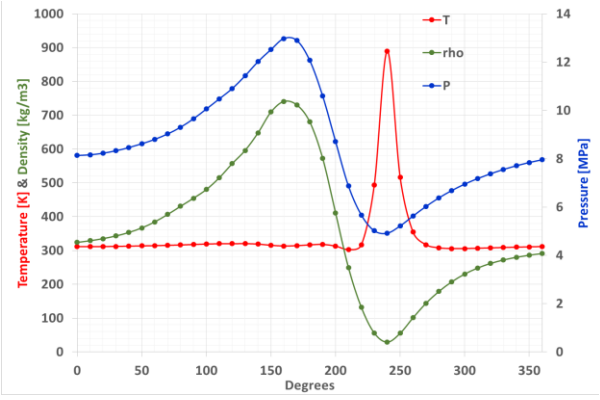


**Figure 8. Bearing temperature distribution calculated from thermodynamic states given in Dousti & Allaire (2016)**

summation of generated hydrodynamic forces for the predicted pressure profiles shown in Figure 6 will result in over predictions. Figure 10 shows such over prediction when comparing their data to predictions for the same bearing made with Heshmat's rigid bearing incompressible solution to Reynolds equation, which accounts for local variations in viscosity and density including the effect of turbulence through the G factor as noted in Eqs (1) and (2). Moreover, in reality, in a rigid pad bearing, as the pressure field attempts to go sub-ambient, a cross-flow from the axial direction would instantly be established, and the load bearing contribution of the sub-ambient portion of the field would be negated, again resulting in the pressure distribution shown in Figure 7

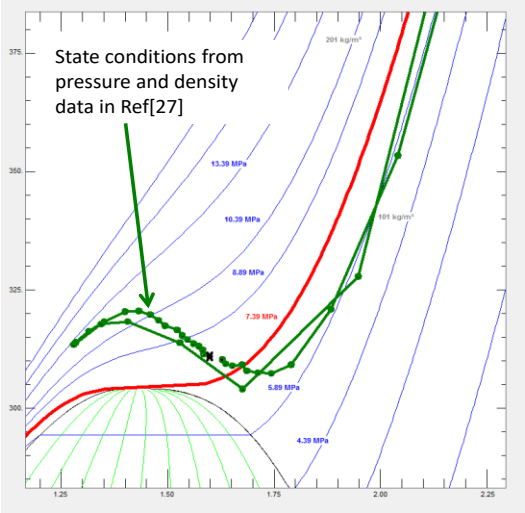


**Figure 9. Calculated thermodynamic states of $CO_2$ in the bearing of Dousti & Allaire (2016)**

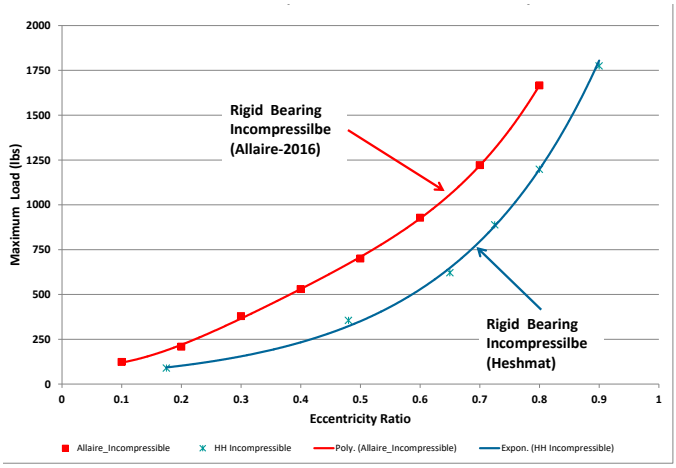


**Figure 10. Comparison of Dousti and Allaire (2016) vs. Heshmat (1988) predictions with incompressible fluid**

## Compressible Compliant Foil Bearing Performance

Given the importance of the hydrodynamic properties to the performance of the bearing, a review of the governing Reynolds equation for compressible media is instructive. Whereas in the incompressible Reynolds equation density is constant, this is not so in the compressible case as seen in the two-dimensional Reynolds equation where the variable fluid density is retained inside the partial differential:

$$\frac{1}{R^2}\frac{\partial}{\partial\theta}\left[h^3\rho\frac{\partial p}{\partial\theta}\right]+\frac{\partial}{\partial z}\left[h^3\rho\frac{\partial p}{\partial z}\right]=6\mu\omega\frac{\partial\rho h}{\partial\theta} \tag{3}$$

In the compressible case, density is related to the pressure by an equation of state of the form: $p = C_g\rho^n$, Where $C_g$ is a constant, *n=1* for isothermal conditions and $n = c_p/c_v$ for adiabatic conditions. The usual situation with a compressible/gas bearing is approximated by the isothermal case so it is assumed that $p = \rho C_g$. After introducing the following non-dimensional parameters $\bar{z} = z/R$, $\bar{p} = p/p_a$, $\bar{h} = h/C$, and $\Lambda = \frac{6\mu\omega}{p_a}\left(\frac{R}{C}\right)^2$, the dimensionless Reynolds equation becomes

$$\frac{\partial}{\partial\theta}\left[\bar{p}\,\bar{h}^3\frac{\partial\bar{p}}{\partial\theta}\right]+\frac{\partial}{\partial\bar{z}}\left[\bar{p}\,\bar{h}^3\frac{\partial\bar{p}}{\partial\bar{z}}\right]=\Lambda\frac{\partial}{\partial\theta}\left(\bar{p}\,\bar{h}\right) \tag{5}$$

By iterative numerical solution of the foregoing equations, it is possible to calculate the pressure field *p* and the film gap *h* distributions. Solutions were obtained for a particular compliant foil journal bearing of dimensions L x D = 40 x 40 mm (where L and D are the bearing length and diameter) in s-$CO_2$ conditions. The CFB is characterized by many operating conditions (load, speed, fluid properties, dynamic and thermal conditions), and by many geometric and structural parameters (overall bearing size, corrugated bump foil

configuration, top smooth foil dimensions and thickness, number of foil layers, foil elastic properties, compliant elements' contact and dislocation points under load, coefficients of friction, etc.). The complex dynamic characteristics of the bearing imparted by these myriad parameters are mathematically expressed by the bearing's compliancy matrix $\alpha_{ijk} = P_a K_{ij}/C_r$, where $P_a$ is the ambient pressure, $K_{ij}$ is the structural stiffness as a function of load and speed parameter, and $C_r$ is the radial clearance. These are all computed via non-linear numerical solution of elasticity equations combined with thin plate analysis including frictional behavior under contact and non-contact situations (Heshmat & Ren, 2010). This, of course varies dynamically in time, as the structural compliant system elements (foils) adjust *or comply* with the load demands of the journal and the varying conditions of the film established during operation. A temporal snapshot of the compliancy matrix for the bearing solution at a given $\alpha_{ij,}\{_k^{th}\}$ iteration is shown in Figure 11. Computation of this matrix is a step in the iterative process in which the structural foils equations and the Reynolds equations are solved by nested FEA within FD analyses until a converged solution is obtained.

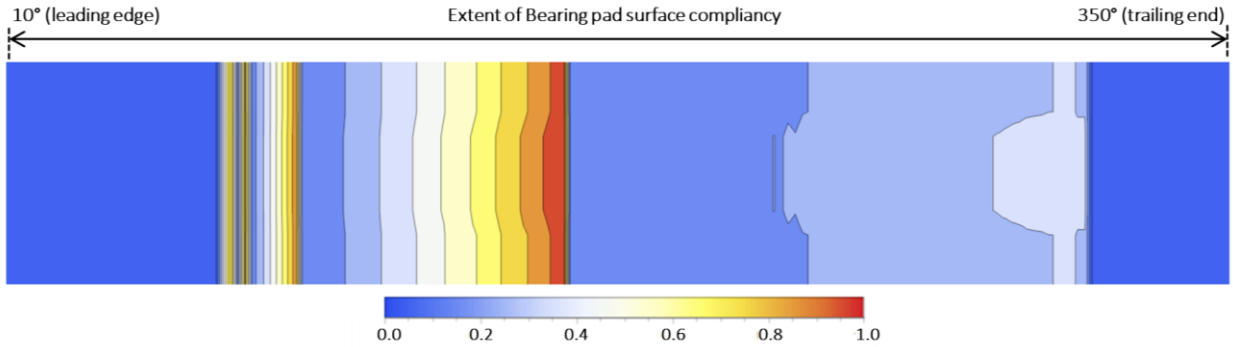


**Figure 11. Instantaneous realization of the compliancy matrix for 40 x 40 mm journal**

The overall solution for the elasto-hydrodynamic problem is shown in Figure 12 and Figure 13. The hydrodynamic pressure field is shown in Figure 12. It reaches a maximum where the film is smallest, but most importantly, one can notice that the field never drops below the ambient pressure, which is consistent with the results shown in Figure 7. Figure 13 shows the associated film-height or bearing gap.

Solutions were obtained for different values of the eccentricity ratio. These are shown along the bearing centerline in Figure 14 and Figure 15, respectively. The distributions are consistent with the results shown in Figure 12 and Figure 13, with the pressure maxima occurring where the gaps reach their minima, and the pressure never dropping below the bearing's ambient pressure. The pressure field is also seen to increase as the eccentricity ratio increases.

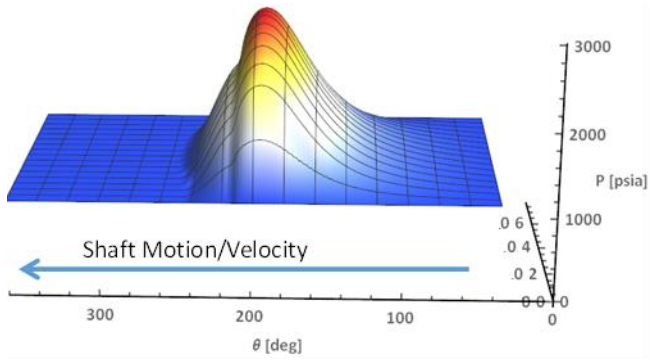


**Figure 12. Pressure profile for s-$CO_2$ foil bearing**

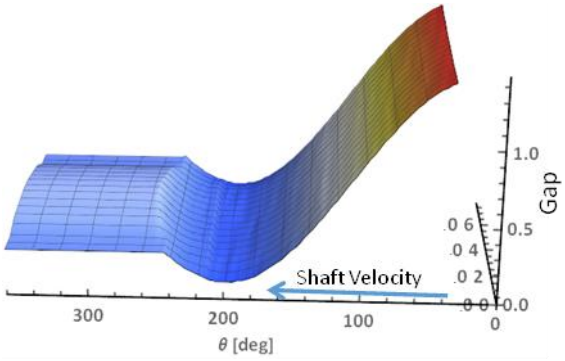


**Figure 13. Predicted s-$CO_2$ CFB film height/gap**

The pressure fields for the different eccentricity ratios can be integrated over the total area of the compliant foils to determine the overall bearing load capacity. Figure 16 shows a comparison between the load capacities calculated in this manner for both a foil and a rigid bearing in s-$CO_2$ at 8 MPa ambient pressure, 60,000 rpm, 40 mm (1.57 inch) diameter for different eccentricity ratios.

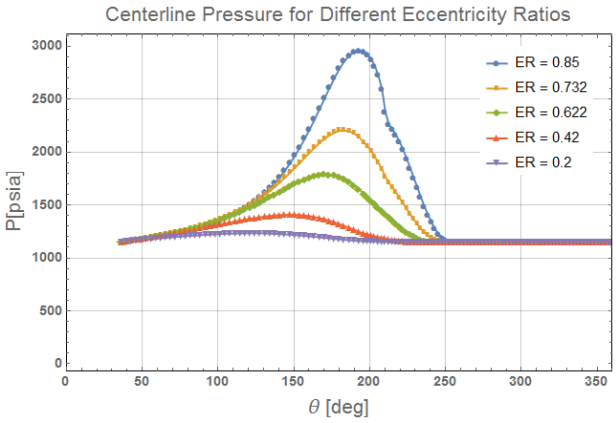


**Figure 14. s-$CO_2$ bearing pressure vs eccentricity ratio**

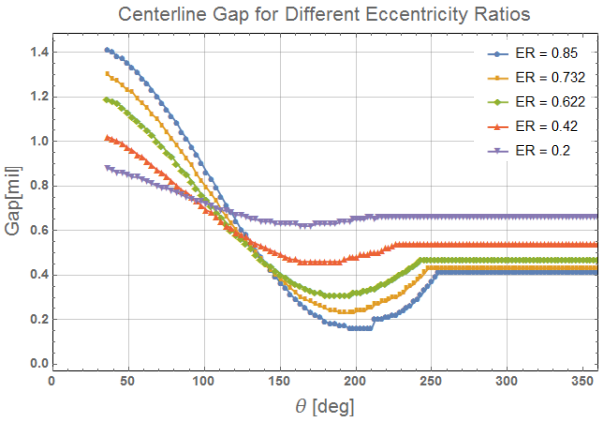


**Figure 15. Gap vs eccentricity for s-CO2 foil bearing**

It is important to emphasize that the pressure never drops below the bearing ambient pressure, in sharp contrast with the results shown in Figure 6. A key feature of foil bearings that allows them to operate in this manner is the fact that the top smooth foil, which is the bearing surface, is only attached to the bump spring structure at one location (see

Figure 17). Being free to move and by having ambient pressure behind the top foil, the foil moves to accommodate and balance out any pressure differentials between the shaft/bearing and top foil/structure. Since the top foil becomes parallel with the shaft no hydrodynamic pressure is generated and pressure equilibrium is achieved. A rigid bearing cannot self-adapt and accommodate such sub ambient pressures, which can result in choked flow, corresponding thermal runaway and failure.

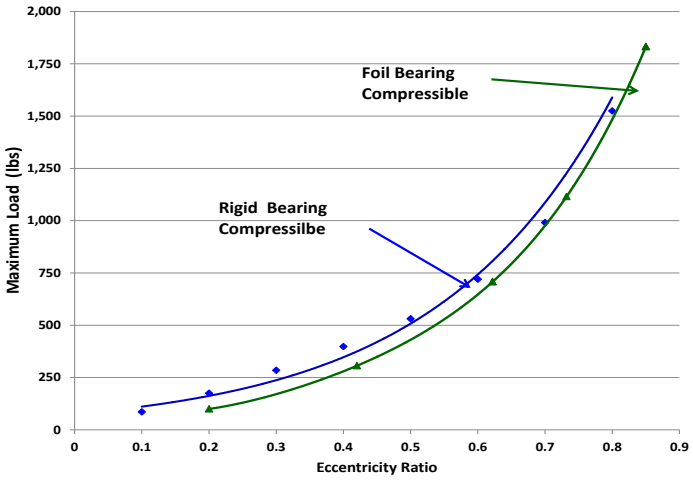


**Figure 16. Foil vs rigid bearing in s-$CO_2$ at 8 MPa ambient press, 60 krpm, D = 40 mm**

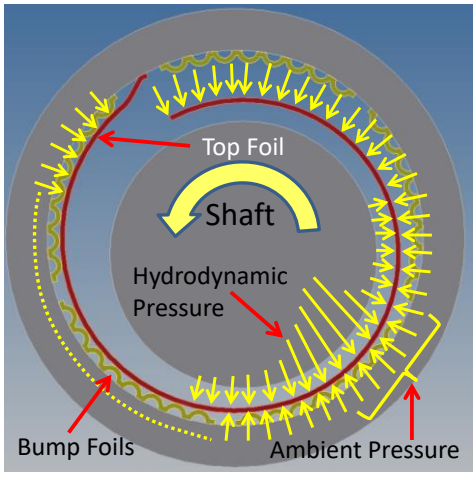


**Figure 17. Foil bearing showing top foil free to move**

## DESIGN OF A 10 MWE RECOMPRESSION S-$CO_2$ SYSTEM

The design process of a turbogenerator power system is an iterative process that is anchored on a typically small number of fixed design conditions provided at the time of problem definition. This process is shown graphically in Figure 18. The process starts with identification of the customer electrical power requirements and with consideration to the characteristics of the available heat sources (e.g., nuclear reactor or high temperature exhaust) and sink conditions (e.g. cooling towers or radiators), which are often outside of the control of the turbogenerator and compressor designer. This leads to the definition of a preliminary cycle operating regime and to selection of the most adequate working fluid for the heat source/sink operating temperatures. Fluid selection and source/sink conditions are then used to determine the pressure and temperature states achievable by the cycle and consequently the available energy for work extraction as a function of the calculated enthalpies. With an assumed flow, predictions of the cycle power extraction are made. The cycle operating conditions are then used as input for the mean line turbomachinery analysis for aero component sizing. In the sizing analysis, both compressor and turbine head and flow coefficients are estimated in an effort to ascertain whether radial inflow or axial flow machinery designs are more appropriate, whether a single or multistage approach must be pursued, and what operating speeds yield peak adiabatic efficiencies. With predicted turbine and compressor adiabatic efficiencies, the overall actual cycle net power is determined. Due to the mismatch between the optimal operating speeds of turbomachinery and that of electrical generators, the field of available generators that are feasible for the application is narrow, and selection of turbomachinery speeds can only be made once adequate gearboxes are identified. Gearbox and other mechanical efficiencies, windage, and electrical losses must be factored to determine if the cycle can supply sufficient shaft power to the generator. The iterative loop is repeated until a satisfactory (optimal) solution is found.

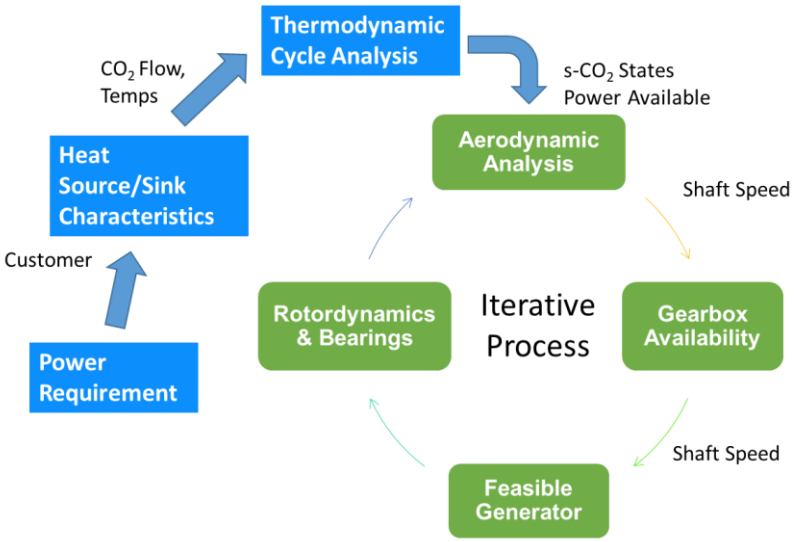


**Figure 18. Iterative turboalternator design process.**

This paper provides a brief discussion on the challenges associated with designing a complete power train for a 10 MWe power generation s-$CO_2$ system. Individual sections and subsections touch upon the elements in the green blocks of Figure 18. Other critical elements to the development of this type of power generation system, like the nature of the heat source, the availability of recuperators, and the means to achieve heat rejection are beyond the scope of the work.

### Cycle Definition

Before sizing of the turbomachinery, it is necessary to define the thermodynamic cycle. The main assumptions made are that the desired electrical power target is 10 MWe, that the system will operate with s-$CO_2$ as working fluid, and that the heat source is robust enough to provide enough heat to maintain a steady turbine inlet temperature (TIT) of 750°C regardless of the designed flow and pressure requirements. The recompression cycle was the preferred s-$CO_2$ power cycle, since it can provide thermal efficiencies in the range of 45-50% for typical s-$CO_2$ operating conditions. Discussion of s-$CO_2$

thermodynamic cycles is beyond the scope of this paper, and the reader is referred to the literature, for example Ahn *et al.* (2015). However a screen capture of the authors' design tool is shown in Figure 19, and it includes a schematic of the re-compression cycle power plant and both the assumed and calculated operating conditions to satisfy the 10 MWe requirements.

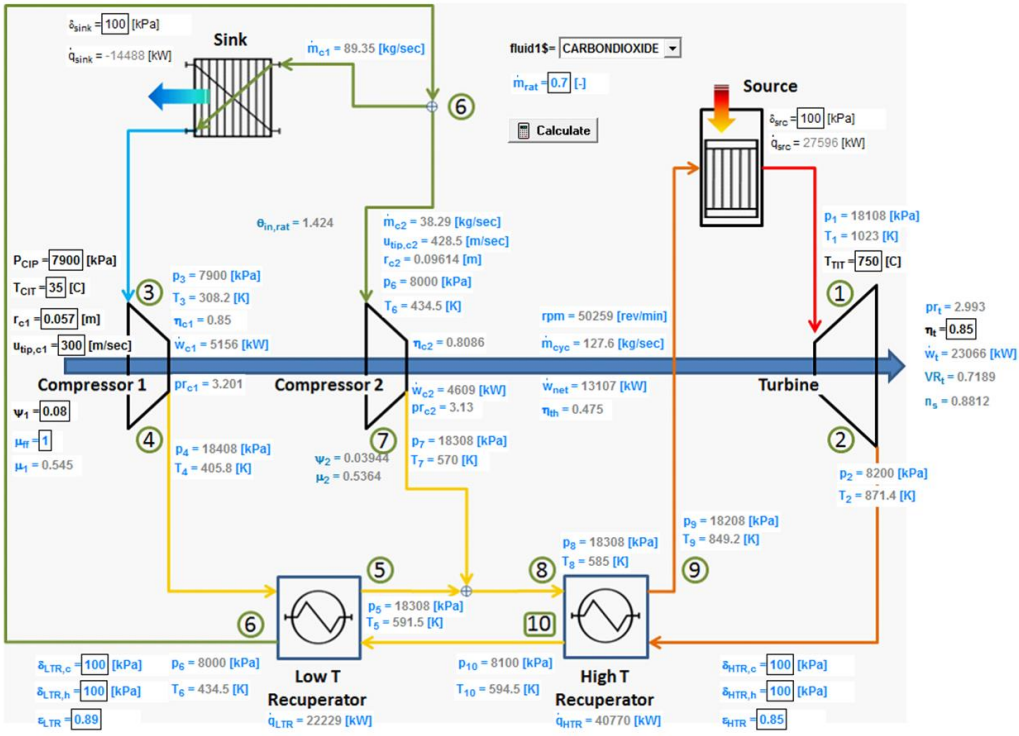


**Figure 19. Baseline design for s-$CO_2$ Brayton cycle with recompression where compressors and turbine are mounted on a single shaft.**

Table 1 shows some of the key design parameters based on the cycle calculations. Given the nature of the supercritical power cycle the compressor inlet pressure was input as a constant, slightly greater than critical pressure of the working fluid. The compressor outlet pressure is not a user output, but is determined by the algorithm and is based on non-dimensional compressor design analysis rules. In the same respect, cycle flow and rotation speed is determined based on non-dimensional flow coefficient and specific speed using techniques described in Balje (1981) and Aungier (2000) that will be discussed below. A key result of the iterative design process is the determination of flow splitting between the two compressors which is selected to be 70/30 between the compressor and the re-compressor (Compressor 1 and Compressor 2 in the diagram). In this initial approach, all the aero machinery, i.e., compressors and turbine(s) are assumed to be mounted on a common shaft thus rotating at the same speed. This will be discussed below in further detail in the context of the power train layout. Assuming mechanical, gearbox, and generator efficiencies are 95%, 96%, and 92%, respectively, the cycle's available shaft power of 12.9 MW can deliver a net electrical power of 11 MWe.

Table 1: Key Cycle Parameters.

| Cycle Parameter | Value |
|---|---|
| Mass Flow | 127.6 [kg/s] |
| Compressor Inlet Pressure | 7,900 [kPa] |
| Compressor Discharge Pressure | 18408 [kPa] |
| Flow Split (Main/Re-compressor) | 0.7 / 0.3 |
| Turbine Inlet Temperature | 750 [°C] |
| Pressure Drop per Element | 100 [kPa] |
| Cycle Thermal Efficiency | 47.5 [%] |
| Rotation Speed | 50,250 [rpm] |
| Shaft Power | 13.1 [MW] |
| Net Electrical Power | 11 [MWe] |

## Power Train Layout

In the previous section, cycle analysis coupled with cursory aerodynamic considerations yielded an operating envelope for the turbomachinery design space. In this section, the layout of the complete power train is taken into consideration. The power train consists of the turbine, generator the gearbox required by the turbine/generator speed mismatch. Several possible layouts are proposed and the pros and cons of each are discussed. For purposes of discussion, it is assumed that the power turbine consists of a split-inlet flow design, symmetric about the midpoint, and that the working fluid enters the machine at the shaft midpoint and flows towards the ends through two stages of expansion, yielding greater than 20 MW shaft power. It is also assumed that both the turbine and compressors are in principle identical across all layout concepts presented and that, regardless of the layout, the thermodynamic behavior of the cycle remains the same. While outside the scope of this paper, the validity of this assumption should be verified in the context of real hardware fabrication, as details like the difference in piping (valves, fittings, pipe bends), the distance between components, the efficiencies of the individual interfaces, and even the differences in thermal insulation may have an impact in a real system.

### Mechanically Coupled Power Train

Figure 20 shows the most basic mechanically-coupled power train (MCPT), which assumes that the power turbine, main compressor and re-compressor run at a common speed, essentially mounted on the same shaft, with a reducing gearbox to drive an induction alternator. The shaft power generated by the power turbine is capable of driving both the main and re-compressor, as well as transmitting enough power to the generator to yield a net 10 $MW_e$ output to the grid. Variations of this configuration are also possible, such as the approach shown in Figure 21, where two smaller 5 MW generators are coupled to the power turbine through a split-output gearbox.

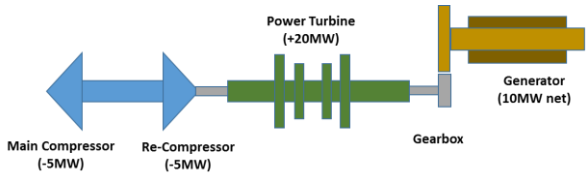


**Figure 20. Basic MCPT concept with one generator**

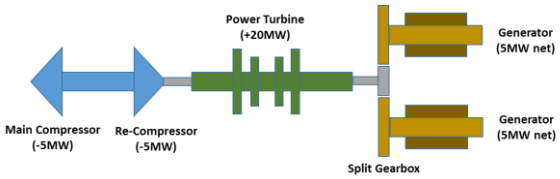


**Figure 21. Split gearbox to drive two alternators**

While the MCPT concepts seem like the most direct and simplified solutions, the overall length of the rotating group presents critical speed and thermal growth challenges that may translate into significant risk. Aside from the details in generators, discussed in a later section, the mechanically coupled power train consists of two compressor stages and multiple turbine stages *all rotating at the same speed on a single shaft*. Attaching so many aerodynamic components to one long rotating group results in a low bending critical speed which may be below the operating speed. Passing through the critical bending speed during startup and shutdown imposes severe loading conditions on bearings and could cause stability issues.

Even if it is possible to operate above the bending critical speed, it is considered that for the application this should be avoided. To this effect, use should be made of *flexible quill couplings* between the power turbine and the compressors shafts. This effectively decouples the dynamics of the compressor shafts and turbine, so that each operate below their respective bending critical speeds (Heshmat, 2014). Thermal gradients across the entire rotating group can also be problematic. Achieving turbomachinery peak aerodynamic performance is largely dependent on the radial and axial locations of the aero components within the shrouding. The high temperature turbine will see large thermal growth during operation. Since thermal growth is directly determined by the length of the geometry under consideration, the length of the MCPT concept amplifies longitudinal thermal growth issues. Another concern is that in the event of a

turbine failure, being all a single rotating group, the mechanically coupled concept would cause simultaneous compressor failure and immediately stop the working fluid flow in the power cycle. This failure could present a risk of thermal run-away of the reactor heat source.

## Electrically-Coupled Power Train

The electrically-coupled power train (ECPT) shown in Figure 22 is a possible strategy to avoid the rotordynamic, thermal growth and risk challenges associated with the mechanically-coupled concept. Here, the power turbine is coupled through a gearbox to an oversized power generator. The electric output is sufficient to drive both compressors via a gearbox-coupled 10 MWe electric motor, resulting in a net 10 MWe grid output. The concept allows for simplified rotating shaft design, however, the system becomes more elaborate, requiring two gearboxes, a larger generator and a separate motor to drive the compressors.

Alternatively, two individual compressors may be considered each requiring approximately 5 MWe input power, as shown in Figure 23 While this concept results in an increased number of system components, the 5 MWe motor power level is more appropriately sized to mate with the highest power and rotating speed of permanent magnet (PM) motors currently available and/or under development.

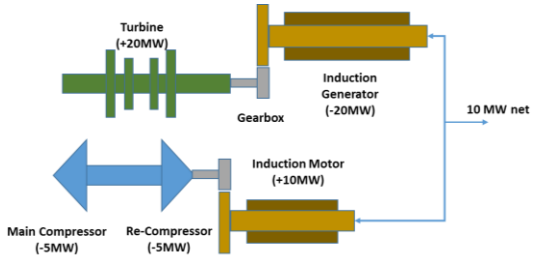


**Figure 22. ECPT with generator driving compressors' motor**

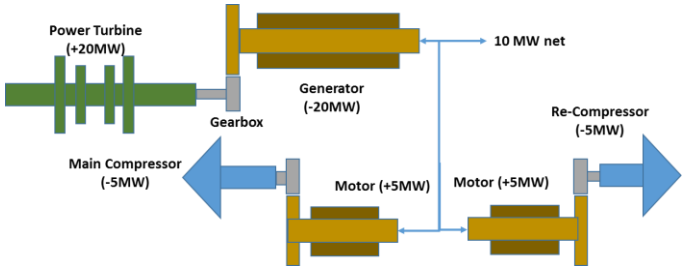


**Figure 23. ECPT with generator driving compressor with individual motors**

The integration of high speed PM motors reduces gear ratios and will improve overall power train efficiency. Additionally, the electrically-coupled layouts offer higher reliability than the mechanically coupled layout as turbine failure does not necessarily result in simultaneous compressor seizure because they are on separate rotors. With an auxiliary power source for at least one of the compressors, this could ensures continued circulation of working flow through the thermal source (at least for the period required to shut it down).

## Independent Turbine Drive

A third power train layout concept is the Independent Turbine Drive (ITD) shown in Figure 24. In this concept, two turbine expansion stages are on two different shafts. Turbine flow travels in series, first through a high-pressure (HP) turbine and then through a low-pressure (LP) turbine. The HP power turbine is connected to a gearbox to drive a 10 MW generator. Flow exiting the HP power turbine travels to the LP drive turbine, which drives the compressor and re-compressor shaft. The individual turbine stages of the ITD layout are identical to those of the multistage power turbines of the mechanically and electrically coupled layout. The compressor shaft, directly coupled to the LP turbine requires no gearbox and improved transmission efficiency is achieved. The turbomachinery is simpler than the MCPT layout as there are two independent rotating groups rather than one. The reduced length drastically improves rotordynamic and thermal growth challenges. The IDT layout is a smaller and more compact design than the ECPT layout as it requires only a single 10 MW generator. In the event of turbine failure, the multiple rotating shafts of the IDT layout offer some reliability, as the compressors do not seize up instantaneously.

A modification of this concept is shown in Figure 25, where the HP turbine discharge is split between two

5 MW LP turbines to drive each the compressor and re-compressor. An advantage of this concept is the independence of the compressors, which introduces a margin of safety in the event of a compressor or compressor drive turbine failure, ensuring that at least one compressor can continue supplying the working flow to the heat source, and avoiding thermal runaway.

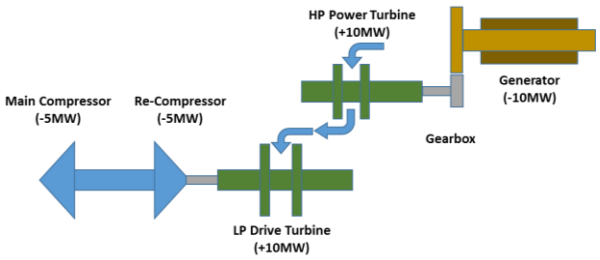


Figure 24. ITD power train with flow path in series

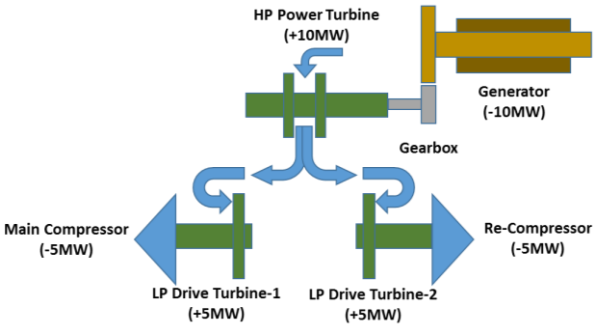


Figure 25. ITD power train with independent LPTs

## Powertrain Component Selection

In the previous section, three power train layouts were discussed, including mechanically-coupled, electrically-coupled and independent turbine drive configurations. In this section, for completeness of the system design discussion, we give a brief overview of viable generators and gearboxes. The information and pictures in this section (specifically Figure 26 through Figure 30) came from conversations with the respective company representatives and/or from their websites.

### Availability of generators for s-$CO_2$ operating conditions

Given the power target of 10 MWe output, the discussion begins with which commercial solutions are available. At the 10 MWe level, no PM generators are available, however several manufactures are available which produce a 10 MW induction generator, for example Baldor Electric (a subsidiary of ABB Inc.), Siemens, and Curtis-Wright. Each offer slightly different solutions. A comparison of each is provided below. Baldor Electric offers a number of multi-megawatt induction generators from 5 to 50 MW, all rotating at 1800 rpm. A list of the sizes and weights available are provided in Table 2. A schematic of Baldor's 10 MW option is shown in Figure 26. Siemens AG (Nurnberg, Germany) was identified as a second manufacturer with commercially available generators in the multi-megawatt power scale. Siemens offers large induction generators rotating at both 1800 rpm and 3600 rpm. The 10 MW induction generator offered by Siemens is shown in Figure 27. The dimensions of this unit are 3.2 m [L] x 1.6 m [W] x 2.4 m [H], and its weight is 20,000 kg. These Baldor and Siemens "off-the-shelf" solutions are bulky and operate at speeds well below that of any potential s-$CO_2$ turbine, thus requiring significant gear reduction. A more advanced generator technology that is better suited to mate with an advanced s-$CO_2$ turbine is available from Curtiss-Wright EMD (Cheswick, PA). They have produced induction generators in the 5-15 MW power scale at speeds of 7000 rpm. A 14 MW Curtiss-Wright generator, shown Figure 28, provides a high power density of 1.36 kW/kg; more than six times the power density of traditional low-speed air-cooled generators. With operating speeds of 7,000 rpm, the required gear turbine to generator reduction ratio could be less than 7:1.

Table 2: Generators from Baldor Electric

| Rating | Frame | Est Weight |
|---|---|---|
| **5 MW** | AMG 0630 | 10,000 kg |
| **10 MW** | AMS 0800 | 21,000 kg |
| **25 MW** | AMS 1120 | 46,000 kg |
| **50 MW** | AMS 1400 | 80,000 kg |

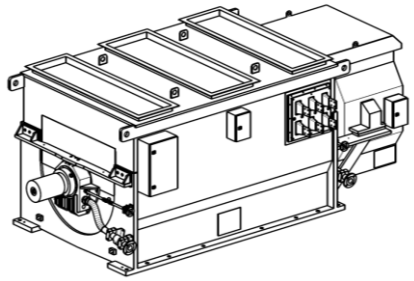

Figure 26. Baldor-ABB 10 MW 1800 rpm induction generator

Figure 27. Siemens 10 MW 3600 rpm induction generator

Figure 28. Curtiss-Wright 14 MW 7000 rpm induction generator

While the multi-megawatt power scale is dominated by induction type generators, there are also a few PM options to consider. Currently no single PM generator is available at the 10 MW power level, however coupling of two or more smaller generators may be considered through use of a split gear box. General Atomics offers an 8 MW generator which operates at speeds up to 15,000 rpm, and this is shown in Figure 29. General Electric is also developing a multi-megawatt generator, which is shown in Figure 30. Both of these larger scale PM generators employ magnetic bearings, which adds significant cost and complexity relative to the mature and commercially available induction motors described above. The General Atomics PM generator has a published mass of 20,000 kg with a height of approximately 4.5 m. Despite the 4-8x increase in operating speed, the unit has similar mass to the Baldor (1800 rpm) and Siemens (3600 rpm) induction type generators. Further details about these PM generators are needed, but it can be assumed that the magnetic bearing components such as the power supply and controller must add significant weight and volume. Still, the permanent magnet motor offers performance benefits, like greater mechanical to electrical conversion efficiency. Additionally, the increased speed reduces reliance on gear reduction and contributes to greater power train efficiency. These factors must all be taken into consideration in a trade-off study when comparing the various powertrain layouts.

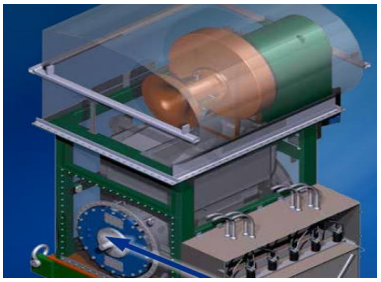

Figure 29. General Atomics 8 MW 15,000 rpm PM generator


Figure 30. General Electric 5 MW 17,000 rpm PM generator

## Gearbox Availability

The speed mismatch between the turbomachinery and available generators requires the availability of robust and efficient gearboxes. We contacted major commercial suppliers of multi-megawatt gearboxes. While no off-the-shelf solutions were identified, a number of groups were found with experience in the approximate power and speed ranges desired. For example, a 20 MW gearbox capable of speeds up to 50,000 rpm was designed and constructed by David Brown Gear Systems Ltd (Hudderfield, UK). Through discussion with the manufacturer, it was possible to identify critical considerations for the adoption of the gearbox technology for a 10 MWe s-$CO_2$ system. For example, in the 1-10 MW power scale, it was revealed that gearbox speed is typically limited to 50,000 rpm, which would should be take into account by the aerodynamic design. The manufacturer also provided estimates for mechanical efficiency to be 98.8% per stage. For large gearing ratios greater than 10:1, two stages would be required. These systems present other parasitic losses not included in this efficiency estimate, such as fluid film bearing losses and auxiliary oil scavenge pumps. The unit weight of this system was 8500 kg (dry weight).

## Turbomachinery Design

In a previous section, several potential layouts for the power train configuration were proposed, including mechanically coupled, electrically coupled and independent turbine drive. Each of these concepts leveraged a common—yet undefined—multi-stage expansion turbine which was the source of shaft power regardless of the layout approach. In addition, two compressors were shown: the main and re-compressors, each vital to the cycle. In this section, the aerodynamic and rotordynamic design methods which were used to size the components is described.

### Power Turbine Aerodynamic Design

Aerodynamic design begins with preliminary sizing of wheels in order to approximate size and rotating speed. The use of specific speed and diameter, as defined by Balje is a common first approach, where specific speed $n_s = \frac{N\sqrt{Q}}{(gH)^{3/4}}$ and specific diameter $D_s = \frac{D(gH)^{1/4}}{\sqrt{Q}}$ using the standard nomenclature of Balje (1981). With the thermodynamic cycle already defined, the state points at inlet and outlet are already prescribed. The selection of appropriate non-dimensional values can be found by referencing Balje's design guidelines. Significant empirical data sets, as shown in Figure 31, are available for non-dimensional parameters guiding the designer towards the best efficiency before entering the more time consuming detailed design phase. This is particularly valuable when evaluating large design matrices.

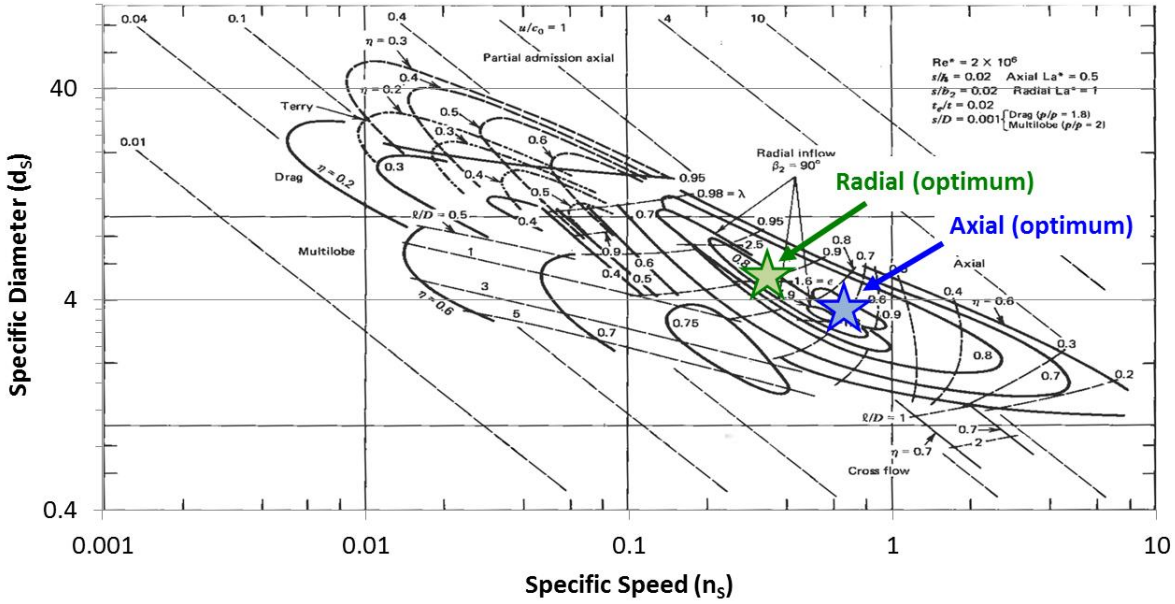


**Figure 31. Selection of ideal non-dimensional turbine specific speed and diameter (Balje, 1981). Optimum radius turbine indicated with green star and axial turbine with blue star.**

For example, in the case of the s-$CO_2$ power turbine, the use of radial and axial turbines, single inlet and split inlet flow schemes, and a variety of expansion steps were all considered. Down selection of these different approaches is first done with non-dimensional analysis and findings are then refined with 1D mean-line analysis software tools. Using the non-dimensional analysis, ideal size and speed parameters for both axial and radial turbine choices determined.

In Table 3, the results of non-dimensional sizing analysis are summarized for the four primary aerodynamic conditions. The results for diameter and rotation speed were most dependent upon flow coefficient and flow configuration (i.e., single inlet or split). Initial estimation regarding the number of expansion stages necessary is first calculated through evaluation of head coefficient in order to assure reasonable enthalpy

per stage is achieved. However more detailed analysis using mean-line analysis was required for this application given the high pressure condition. Such large pressure drop within the turbine stage results in large pressure differential on the blading. Both tall profile axial blades (typical with single inlet configuration) and radial turbine blades are subjected to greater stress. Stress effects on materials are further amplified due to the temperature of operation at the turbine inlet (>700°C). Therefore, more expansion steps are needed. For this reason, the split inlet axial blade allows fewer expansion steps and yields a more compact shaft design.

**Table 3: Results of non-dimensional analysis for s-CO2 power turbine.**

| | Ideal Diameter | Ideal RPM | Number of Stages | Comment |
|---|---|---|---|---|
| **Axial Turbine Split Inlet** | **5-6”** | **50,000** | **2-3** | **Most compact solution with balanced thrust** |
| **Axial Turbine Single Inlet** | **8-9”** | **30,000** | **3-4** | **Large Thrust Forces Generated** |
| **Radial Turbine Split Inlet** | **9-10”** | **25,000** | **4-6** | **Significant shaft length required relative to axial** |
| **Radial Turbine Single Inlet** | **12-14”** | **15,000** | **6-8** | **Large Thrust Forces** |

## Compressor Aerodynamic Design

Using similar design methodology for the compressor, appropriate size and speed design targets were evaluated for both axial and radial turbomachinery. This analysis is conducted for the main compressor (88 kg/s) and a re-compressor (38 kg/s). In Figure 32, ideal operating conditions, again according to Balje non-dimensional empirical analysis, are shown for the main compressor conditions. It can be seen that optimal solutions can be achieved for both types, but the required operating speed of the single stage axial compressor is much greater than that of the single stage radial type. A similar result was achieved when evaluating the re-compressor conditions. These findings are summarized in Table 4.

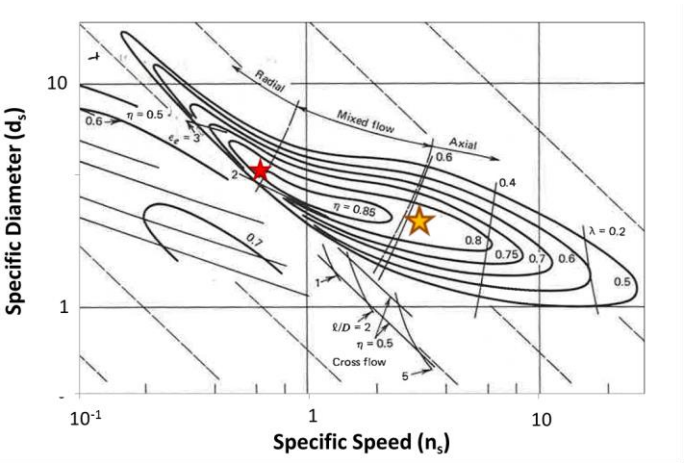


**Figure 32. Non-dimensional empirical performance chart for single stage compression (Balje, 1981).**

In addition to aerodynamic considerations, many other factors must be evaluated during the iterative turbomachinery design, such as integration with other components of the power train. Research in the gearbox capabilities revealed no available technology above 50,000 rpm at the multi-megawatt power level. Another consideration is that the high-speeds of the axial turbine design would yield much smaller shaft size. As a result, much smaller bearing area is available. Given the high operating pressures of this application, small pressure imbalance will yield thrust imbalances on the order of hundreds to thousands of Newton making the small shaft design infeasible. For these reasons, operating speeds above 50,000 rpm

**Table 4: Results of non-dimensional analysis for s-$CO_2$ compressor and re-compressor.**

| | Ideal Diameter | Ideal RPM |
|---|---|---|
| **Radial Turbine – Main Compressor** | 5.25” | 50,000 |
| **Radial Turbine – Re-compressor** | 4.5” | 80,000 |
| **Axial Turbine – Main Compressor** | 2.75” | 300,000 |
| **Axial Turbine – Re-compressor** | 2” | 500,000 |

are not well suited for this application. Reducing speed of the axial concept would necessitate multiple stages of compression. The operating temperatures of the compressor are much lower than those of the turbine. Therefore, blade stress in the compressor is less of a concern allowing the radial compressor to be considered.

## Power Turbine Mechanics

The power turbine drives the s-$CO_2$ power cycle. In all the power train layouts discussed above, a split-flow axial turbine is assumed. In the MCPT and ECPT layouts, the turbine wheels are on a single shaft with 2-stage split flow path. In the ITD layout, the turbine wheels are on different shafts with a single turbine stage on each shaft. Regardless of layout, the blades themselves remain the same. This section focuses only on the MCPT/ECPT turbine design process.

The full rotating assembly of the two-stage power turbine is shown in Figure 33. This shaft configuration is sized to meet the power requirements of the mechanically coupled and electrically coupled power trains. The working fluid enters at mid-shaft as indicated by the green arrows. The flow splits with two equal flow rates traveling towards either end of the shaft. This split flow configuration will inherently negate axial forces resulting from pressure drop within the turbine stage. We have previously shown (Heshmat *et al.*, 2010) that a split flow configuration is preferred in multi-stage turbomachinery supported on foil bearings. In addition to the turbine wheels, two journal surfaces are provided with a diameter of 2.5" for journal foil bearings. In order to address transient and residual axial thrust that may occur, a thrust disk with 6" diameter is located at one end of the shaft. Additional length is provided for foil shaft seals before coupling the drive end of the shaft to the gearbox at the other end.

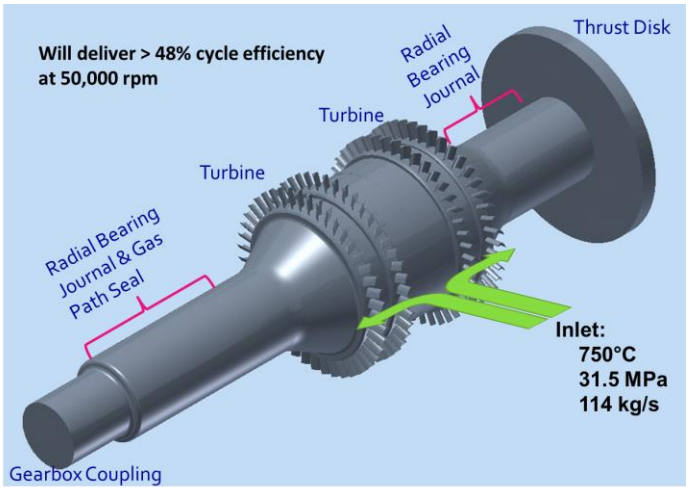


**Figure 33. Rotating shaft for a two-stage power turbine.**

### *Stress Analysis and Material Selection*

Given the high rotation speeds and elevated temperature environment, material selection for the rotating group is a critical design consideration. Figure 34 shows a comparative chart of the ultimate tensile strength (UTS) for sixteen possible materials is shown. The chart is annotated with a green dashed line corresponding to a 100 ksi (690 MPa) stress which is considered a sufficient design criterion for acceptable ultimate tensile stress.

With this, a FEA-based rotating stress analysis is performed for the high pressure turbine, which is the most critical given its direct exposure to 750°C gases. The results

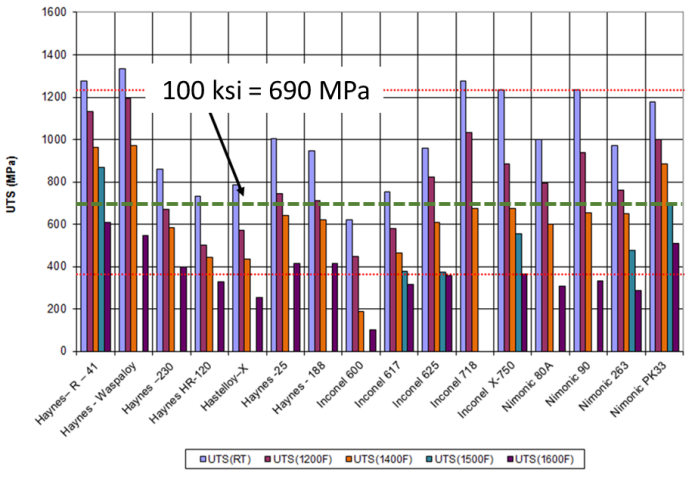


**Figure 34. Review of ultimate tensile strength for various candidate materials at different temperatures.**

of the analysis, shown in Figure 35, using Inconel 718, show that the maximum stress occurring at the thrust disk attachment to the shaft is less than 86 ksi (593 MPa). The ultimate tensile stress of Inconel 718 at 750°C is 120 ksi, leaving sufficient margin for safe rotor operation

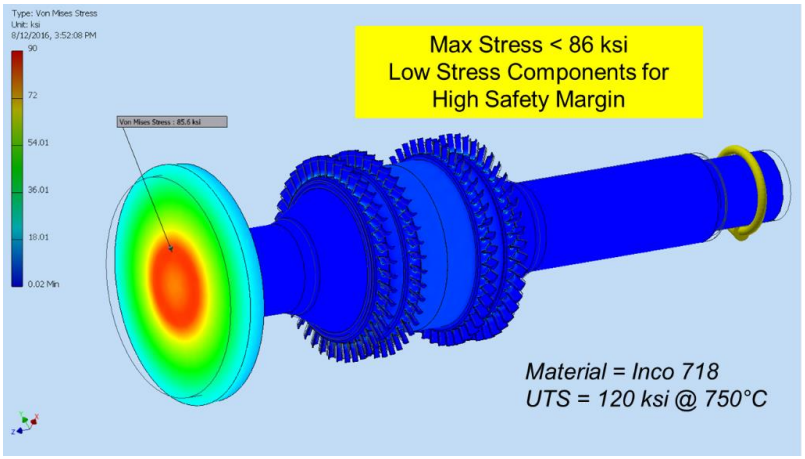


**Figure 35. Stress analysis of the rotating shaft using 3D FEA analysis.**

### *Rotordynamics*

Rotordynamic analysis was performed in order to determine the critical speeds and the stability of the rotor throughout the range of operating speeds. The results of the analysis are also used iteratively to design the foil bearings adequate for the rotordynamic characteristics of the system.

By using a combination of in-house and commercial rotordynamics analysis software, it was determined that both of the rigid body modes (conical and translatory) fall well below the operating speed range, but this is expected and easily handled by the foil bearings. Where care must be exercised is in ensuring that the first bending critical speed lies well above the maximum expected system operating speed, as this ensures a stable and robust operation of the turbine. The analysis predicted that this mode occurs at 93000 rpm, which is well above the nominal 50000 rpm operating speed. Results from the 3D-FEA analysis are shown in Figure 36.

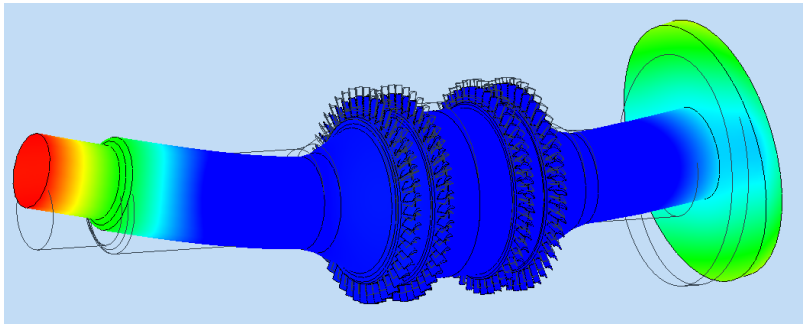

**Figure 36. First bending mode of the rotating group determined to be 93,000 rpm using 3D FEA modal analysis.**

### *Foil Bearings*

With the shaft geometry, weight, center of mass, and moments of inertia determined, and with the rotordynamic analysis complete, it is possible to design the foil bearings to deliver the stiffness and damping required for stable rotordynamics. The shaft journal diameter is 2.5”, and the bearing length is defined to be 2.5”, resulting in an effective area of 6.25 $in^2$, where bearing area is defined as Length x Diameter. Given an estimated static load of 27-28 $lb_f$, the resulting specific bearing load is 4.3-4.5 $lb/in^2$. Following best design practices, foil bearings are normally sized to carry 3-5 $lb/in^2$ static load. Maximum specific load capacity of Gen 5 foil bearings at full speed operation has been demonstrated to be up to 100 $lb/in^2$. For this application, the absolute load capacity is therefore 625 $lb_f$, more than 10x the total shaft weight. Therefore results indicate that a foil bearing of 2.5” diameter is well suited for the power turbine. An example of this bearing design is shown in Figure 37.

The proposed split-flow inlet for the power turbine was selected primarily for the inherently reduced thrust forces. However asymmetry in the shaft results in pressure variation and some residual thrust force will result. A pair of double-acting thrust foil bearings, such as those shown in Figure 38, are required to mitigate the thrust imbalance.

**Figure 37. Example of a MITI 2.5" diameter foil journal bearing, similar to that required for the 10 MW s-$CO_2$ application.**

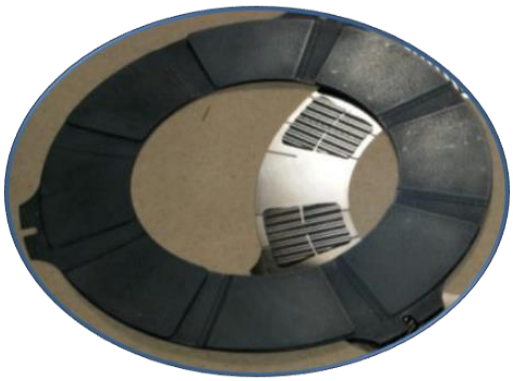

**Figure 38. Example of a MITI 6.0" diameter foil thrust bearing, similar to that required for the 10 MW s-$CO_2$ application.**

Given the rotation speed of 50,000 rpm, the preferred thrust bearing outer diameter would be on the order of 6.0". This results in an effective thrust bearing area of approximately 21 $in^2$.

The distinction between Gen 5 and Gen 6 bearings lies primarily in the temperature rating of their coatings. For the compressor-side gas paths, Gen 5 bearings with Korolon 900 coatings are adequate, since they are rated to withstand 480°C (~900°F) and the highest compressor discharge temperature is no greater than 297°C. For the turbine-side gas paths characterized by a turbine inlet temperature of 750°C, the Gen 6 bearings are to be used, as their Korolon 1350 and 2250 coatings, with their primarily ceramic composition have been tested to withstand up to 870°C (1600°F) turbine inlet temperatures (Heshmat *et al.* 2010, Heshmat & Walton, 2018).

## Overall Power Turbine Layout

The overall layout of the power turbine is shown in Figure 39. The figure shows the housing, the position of the bearings with respect to the rotating element and indicates the position of the primary flow inlet and outlets, as well as the secondary flows. Design process details of these turbine elements are beyond the scope of this paper, but it should be noted that it is critical that the housings materials selection must consider the operating temperatures, and will likely involve nickel-based super alloys (e.g. Inconel X-750). Additionally, the thicknesses must be calculated to hold the extreme operating pressures.

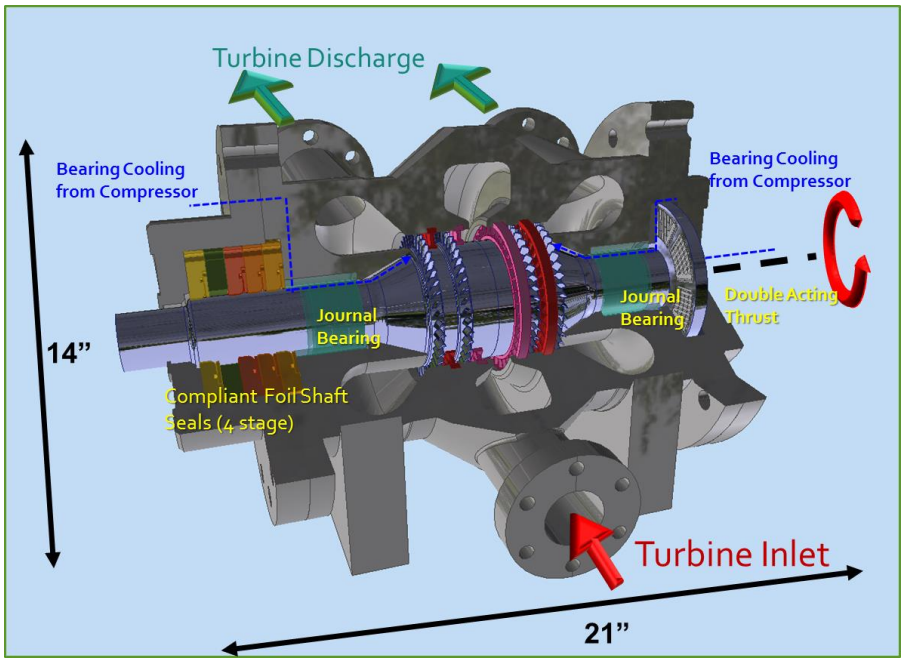


**Figure 39. Power turbine for s-$CO_2$ power cycle with proposed shafting, housing and critical flow paths**

## Overall System Layout

In order to give an idea of the size of a 10 MWe powertrain, Figure 40, Figure 41, and Figure 42 show renderings of the overall configuration based on the elements described in the sections above. All three figures show the mechanically coupled option (as this gives an idea of the potentially largest scale of the system footprint). Only the power turbine is included as it relates to the gearbox and the generator. The compressors are not shown. Additionally, it is important to note that this excludes any other critical equipment like recuperators, which are beyond the scope of this paper.

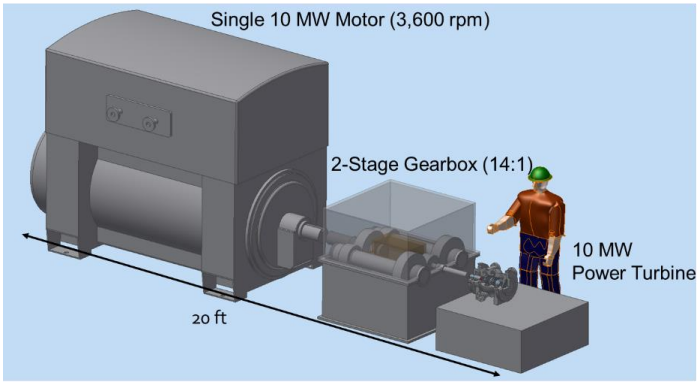


**Figure 40. Mechanically coupled power train layout with single 10 MW induction generator.**

Figure 40 shows the system built with the commercially available Baldor, Inc. induction generator. Such a design would require a 2-stage gearbox to achieve a 14:1 reduction between the power turbine and the generator. Figure 41 shows the layout based on the Curtiss-Wright water-cooled induction generator. Finally, Figure 42 shows the option with GE's dual 5kW permanent magnet generators. The latter presents the smallest footprint for the system.

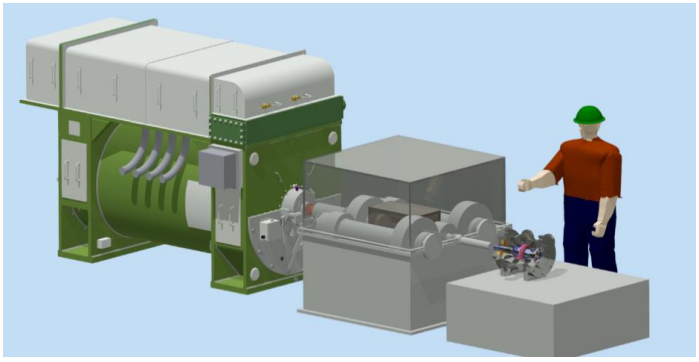

**Figure 41. Mechanically coupled power train layout with dual 7,000 rpm water-cooled induction generator.**

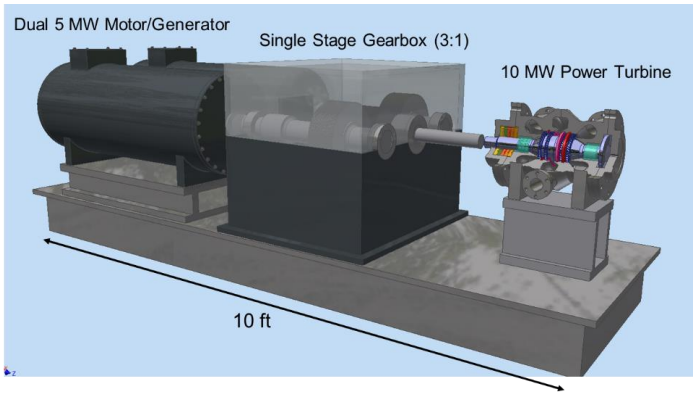


**Figure 42. Mechanically coupled power train generator layout with dual 5 MW permanent magnet generator.**

## Technology Scalability

In addition to viability and technology availability, one of the main questions driving this research is the issue of design scalability in the 3 to 300 $MW_e$ range. As already shown, practical limitations to scalability are imposed by current generator and gearbox technologies. A principal constraint to an s-$CO_2$ generation system is the mismatch between the power cycle/turbomachinery optimal rotating speeds and the maximum speeds allowable by the power generators, resulting in the need for complex gearboxes. Ultimately, for any given power requirement, the gearbox-generator pairing is what limits the maximum speed of the turbomachinery, and thus the maximum electrical powers achievable are set by the ability to combine and parallelize generators into multiunit banks. As discussed, the level or maturity of gearboxes and generators varies, and depending on the selected technologies, practical options are or may be soon becoming available to reach the 100+ MW levels. Alternatively, if larger gearboxes are not suitable, tradeoffs between efficiency and direct drive speeds that are suitable for generator operations will be necessary. Additionally, while

beyond the scope of this work, the availability of recuperative heat exchangers remains a challenge due to the need to contain high differential pressures with large temperature gradients at high absolute temperatures (See for example Carlson *et al.* 2014).

The question remains, however, as to whether the fully integrated turbomachinery system itself including bearings and seals can be developed to broadly satisfy the 3 to 300 $MW_e$ power range. The answer to this lies in the oil-free compliant foil bearing system, which is the center of the turbomachinery and overall support structure and which is arguably the most critical scalability-enabling technology. As previously discussed, the use of oil-free compliant foil bearings altogether eliminates the need for lubrication-support infrastructure (and its scaling), like oil filters and scavenging pumps which add complexity to the system, as well as the need for oil cooling and coking prevention mechanisms. This results in essentially maintenance free rotors, and significantly extends the life of the turbomachinery. Thus, so long as the bearings can be made to support higher power systems, the overall concept can be scaled to larger capacity.

Figure 43 shows a sampling of MITI's experience with the scalability of compliant foil journal bearing designs for different power capacities. The red symbols represent the shaft power of individual engines and the blue symbols the diameters of their journal bearings, and both are plotted against the rotation speed. The curves are the corresponding fits to the individual data. From the data, it can be clearly seen that both metrics scale as an inverse power of rotation speed.

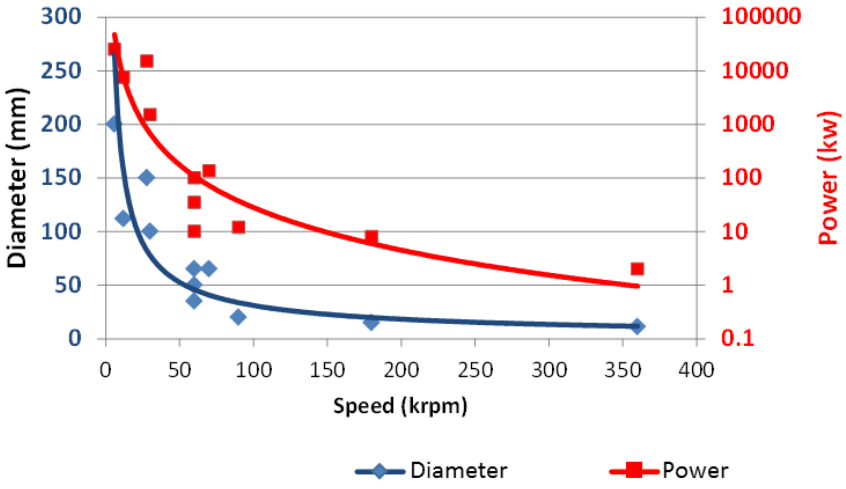


**Figure 43. Turbomachinery power level and required rotor bearing dimension as a function of rotational speed.**

Figure 44 illustrates the relationship between the system generated electrical power, the rotating speed of the power turbine shaft, and the size of the compliant foil bearings required. The orange curve shows that the required journal diameter grows as a weak function of the generated electrical power (diameter $\propto$ power^1/2), and consequently, the maximum possible rotation speed must decrease. It has been demonstrated that a single 100 MWe shaft can be supported by Gen 5 CFBs in the 150 mm diameter range. However, as the electrical power required is larger and the shafts rotate slower and become heavier, it becomes necessary to introduce hybrid bearing system such as magnetic/compliant foil bearings to support the rotors, particularly during start/stop conditions.

It is important to mention that at the conditions of the turbine secondary flow path, the thermodynamic state properties of s-$CO_2$ as a lubricating medium are such that the s-$CO_2$-lubricated bearings have a load capacity that is up to 7.5 times higher than that of their counterparts operating in air at atmospheric conditions.

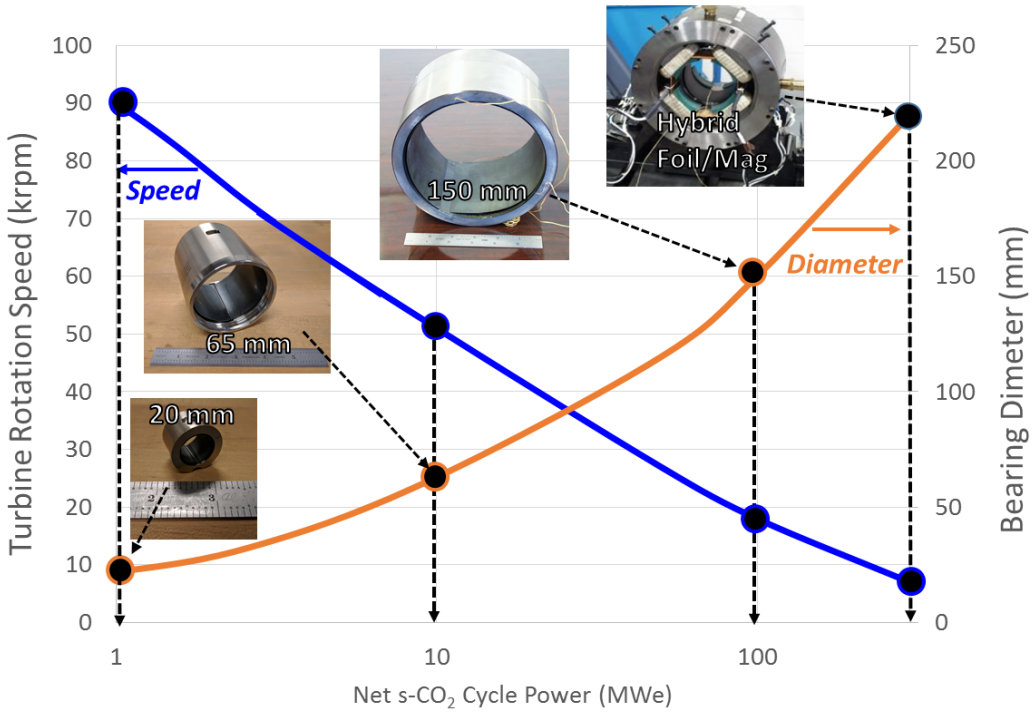


**Figure 44. Power turbine rotor bearing dimension and required rotational speed as a function of system power.**

## DESIGN OF A DYNAMIC S-$CO_2$ CFB TEST SYSTEM

This section presents a preliminary design of a dynamic test system to characterize the rotordynamic and thermal performance of Gen 5 and Gen 6 CFBs that will accommodate full-scale components, and will operate using s-$CO_2$ at realistic speeds, loads, pressure and temperature. The entire rig will be housed in a hermetically sealed enclosure to allow pressurization of the working fluid and recirculating flow such as was used in a prior hydrogen compressor test facility (Heshmat et al. 2010).

Figure 45 shows the layout of the s-$CO_2$ CFB rotordynamic performance characterization engine, which consists of an electrical drive motor coupled to a turbine simulator. The turbine simulator rotor is dynamically identical to an actual power turbine rotor like the one shown in Figure 33, with the only difference being that its aerodynamic wheels are solid disks (not bladed) but maintain the same polar to transverse mass moment of inertia ratio of the turbine rotor. The rotor operates on compliant foil journal bearings designed for operation in $CO_2$. Referring to the figure, the left hand side of the simulator is supplied with actual supercritical $CO_2$, so that the journal bearing operates in a realistic s-$CO_2$ environment. As the gas flows through the bearing and seals, and over the rotor, it loses pressure, so that the right hand side bearing operates in high temperature $CO_2$. The turbine simulator rotor is coupled to the motor via a flexible coupling to decouple the modal responses of the motor and the simulator.

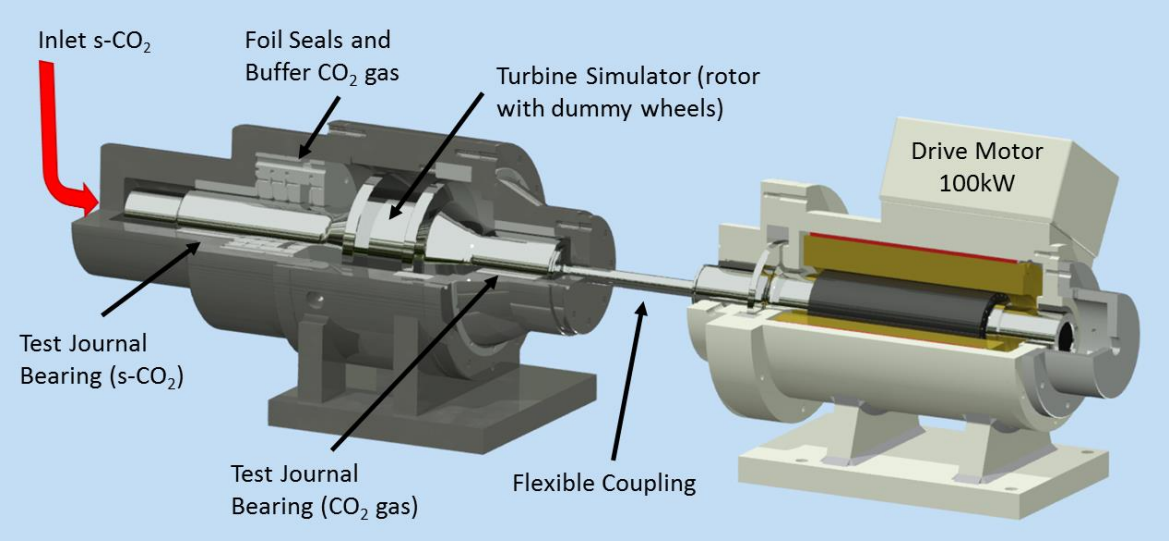


**Figure 45. s-$CO_2$ CFB rotordynamic performance characterization engine.**

The turbine simulator, shown in cross-section in Figure 46, will be heavily instrumented, with thermocouples, pressure transducers, and impedance displacement probes to monitor all its relevant thermodynamic and rotordynamic state variables, thus allowing to fully characterize the performance of the bearings in the presence of the strenuous conditions of a realistic s-$CO_2$ environment.

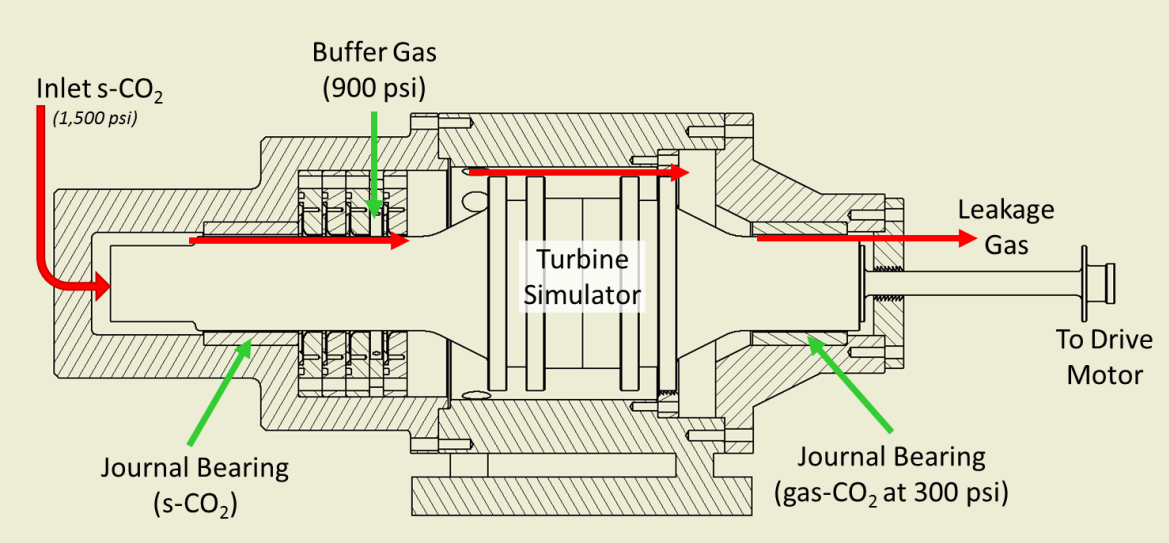


**Figure 46. s-$CO_2$ CFB rotordynamic performance characterization engine cross-section and instrumentation.**

Figure 47 shows a simple schematic of the overall rig including the supply of s-$CO_2$ at the temperatures and pressures required to perform the tests. From left to right in the figure, a bottle of liquefied $CO_2$ fitted with a dip tube will be pressurized by bottled helium to reach 17.2 MPa (2500 psi). The high pressure will be sent via a pressure regulator into an air/$CO_2$ heat exchanger, where the $CO_2$ will be heated to a supercritical state. The s-$CO_2$ will then flow into the turbine simulator module, where it will serve as the operating medium for the first journal bearing. As the flow continues through the seals and down the shaft, it will lose pressure, thus reaching the second journal as high temperature (though not supercritical) $CO_2$. In this manner, the dynamic and tribological behavior of the journal bearings in both supercritical and gaseous CO2 will be explored.

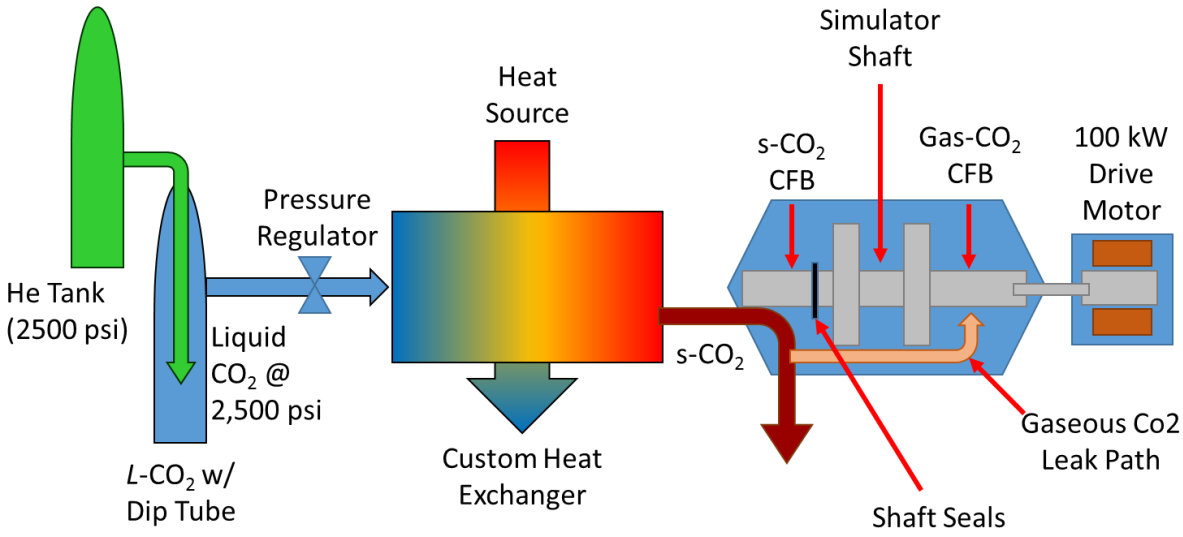


**Figure 47. s-$CO_2$ bearing and rotordynamic performance characterization test rig.**

## CONCLUDING REMARKS

This paper has re-visited the physics governing CFBs in an attempt to offer an improved understanding of their rheological and tribological behavior when operating in s-$CO_2$ turbomachinery. It has also aimed to provide information to assist in better understanding of the design elements required to integrate practical s-$CO_2$ turbomachinery systems for power conversion, and to explore their scalability in the 3 to 300 MW class range. To this effect, a 10 $MW_e$ baseline power plant incorporating all the key subsystems of a recompression s-$CO_2$ Closed Brayton Cycle (CBC) has been analyzed. The main focus of the work is on the design and development of the oil-free Compliant Foil Bearing-based (CFB) turbomachinery required to power the system. Emphasis was made on the design and sizing of the power turbine, including selection of an axial dual entry configuration, as this is the component subjected to the most strenuous operating conditions. Sizing and configuration of possible compressor and re-compressor options are also provided. A number of power train configurations (turbine-gearbox-generator coupling) were also presented and their pros and cons discussed. Other critical elements are also discussed, like bearing sizing and shaft stress and rotordynamic performance. Additionally, considerations regarding sizing and selection of viable electrical generators and the gearboxes required to couple them to the power turbine. With all the design elements presented, scalability of the system is generally addressed in the context of the integrated system but in particular in relation to the use of oil free compliant foil bearings, which are arguably the most critical scalability-enabling technology. The use of oil-free compliant foil bearings altogether eliminates the need for lubrication-support infrastructure, like oil filters, dynamic seals for prevention of lubricating oil contamination by s-$CO_2$, and scavenging pumps which add complexity to the system, as well as the need for oil cooling and coking prevention mechanisms. This results in essentially maintenance free rotors, and significantly extends the life of the turbomachinery. Thus, so long as the bearings can be scaled to support higher power systems, the overall concept can be scaled to larger capacity. Finally, a design is presented to develop a test rig to perform real-time monitoring of the thermodynamic and rotordynamic state variables of a turbine simulator operating in realistic s-$CO_2$ environment, thus allowing to fully characterize the performance of the rotor/bearings assembly in such strenuous conditions. We expect that this work will lay the foundation to ultimately demonstrate the immediate viability of $5^{th}$ and $6^{th}$ Generation CFBs as an enabling technology for s-$CO_2$ power generation.

## REFERENCES


Pasch, J., et al. "Steady State Supercritical Carbon Dioxide Recompression Closed Brayton Cycle Operating Point Comparison With Predictions," *ASME Turbo Expo 2014: Turbine Technical Conference and Exposition*. GT2014-25777, (2014).

Kalra, C., et al. "*Development of High Efficiency Hot Gas Turbo-Expander for Optimized CSP Supercritical CO2 Power Block Operation,*" The 4th International Symposium - Supercritical CO2 Power Cycles (2014)

Talbot, D., "Desk-Size Turbine Could Power a Town," *MIT Technology Review*, (2016)

Fleming, D.D., et al. "Scaling Considerations for a Multi-Megawatt Class Supercritcal CO2 Brayton Cycle and Commercialization," SAND2013-9106. (2013)

Heshmat, Hooshang, Zhaohui Ren, Andrew Z. Hunsberger, James F. Walton, Said Jahanmir, "On the Design of a Multi-Megawatt Oil-Free Centrifugal Compressor for Hydrogen Gas Transportation and Delivery – Operation beyond Supercritical Speeds." *Proceedings of the ASME International Mechanical Engineering Congress*. (2010).

Heshmat, Hooshang, Zhaohui Ren. "The Emergence of Compliant Foil Bearing and Seal Technologies in Support of 21st Century Compressors and Turbine Engines." *ASME 2010 International Mechanical Engineering Congress and Exposition*, 5 (2010).

Heshmat, H. and Walton II, J.F., "*Innovative High-Temperature Compliant Surface Foil Face Seal Development*," AIAA/ASME/SAE/ASEE Joint Propulsion Conference, (2008).

Jahanmir, S., Heshmat, H. and Heshmat, C.A., "*Assessment of Tribological Coatings for Foil Bearing Applications*," (2009) STLE Tribology Transactions, Volume 52, No. 2, pp. 231-242.

Heshmat, H. and Jahanmir, S. "*Evaluation of Coatings for a Large Hybrid Foil/Magnetic Bearing*," ASME Paper IJTC2006-12328, International Joint Tribology Conference, October 23-25, 2006, San Antonio, Texas, (2006).

Heshmat, H., Hryniewicz, P., Walton II, J.F., Willis, J.P., Jahanmir, S. and DellaCorte, C. "*Low-Friction Wear-Resistant Coatings for High-Temperature Foil Bearings*," (2005) Tribology International, Volume 38, Issue 11-12, pp. 1059-1075.

Heshmat, H. "Major Breakthrough in Load Capacity, Speed and Operating Temperature of Foil Thrust Bearings," Proceedings of the World Tribology Congress III – (2005), pp. 111-112.

DellaCorte, C. and Valco, M.J. "*Load Capacity Estimation of Foil Air Journal Bearings for Oil-Free Turbomachinery Applications*," (2000) ARL-TR-2334

Heshmat, H. and Hryniewicz, P. "*Advancing the Load Capacity and Operating Temperature of Foil Thrust Bearings*" (2004) Bulletin of the Polish Society of Tribology (Tribologia), Volume 35 (3), pp.145-157.

Salehi, M., Heshmat, H. and Walton II, J.F. "*Advancements in the Structural Stiffness and Damping of a Large Compliant Foil Journal Bearing – An Experimental Study*," (2007) Journal of Engineering for Gas Turbines and Power, Volume 129 (1), pp. 154-161

Heshmat, H., Shapiro, W. and Gray, S. "*Development of Foil Journal Bearings for High Load Capacity and High-Speed Whirl Stability*," (1982) Journal of Lubrication Technology, ASME Transactions, Volume 104 (2), pp. 149-156

Heshmat, H. "Palier Ae'rodynamique a' film fluide," European Patent Office; Patent No. EP 0601624 B1, (1993)

Heshmat, H. "Advancements in the Performance of Aerodynamic Foil Journal Bearings: High Speed and

Load Capability," (1994) Journal of Tribology, Volume 116 (2), pp. 287-295.

Dousti, Saeid, Paul Allaire, "A Compressible Hydrodynamic Analysis of Journal Bearings Lubricated with Supercritical Carbon Dioxide." 5th International Symposium - Supercritical CO2 Power Cycles. (2016)

Reynolds, O., "*On the Theory of Lubrication and Its Application to Mr. Beauchamp Tower's Experiments,*" Phil Trans. Roy. Soc., (1886)

Sommerfeld, A., "*Zur Hydrodynamischen Theorie der Schmiermittelreibung,*" Z. Math. U. Physik, (1904)

Pinkus, O., and Sternlicht, B., *Theory of Hydrodynamic Lubrication, McGraw Hill Book Company, Inc. (1961)*

Heshmat, H. and Artiles, A. "Analysis of Starved Journal Bearings Including Temperature and Cavitation Effects," (1985) Journal of Tribology, Volume 107 (1), pp. 1-13.

Heshmat, H. "Starved Bearing Technology: Theory and Experiment." PhD Thesis, Mech. Eng. Dept. Rensselear Polytechnic Institute. Troy, New York. (1988)

Heshmat, H. "*The Mechanism of Cavitation in Hydrodynamic Lubrication*," (1991) Tribology Trans, Vol. 34 (2), pp. 177-186.

Ahn, Yoonhan, S.J. Bae, M. Kim, *et al*. "Review of Supercritical $CO_2$ Power Cycle Technology and Current Status of Research and Development." *Nucl. Eng. Technol.* **47**, 647-661. (2015)

Balje, O. E. *Turbo-Machines, a Guide to Design, Selection and Theory*. Wiley & Sons. (1981).

Aungier, R. H. *Centrifugal Compressors, a Design Strategy for Aerodynamic Design and Analysis.* ASME Press. (2000)

Heshmat, Hooshang, James F. Walton, Andrew Hunsberger. "Oil-Free 8 kW High-Speed and High-Specific Power Turbogenerator." *ASME Turbo Expo 2014: Turbine Technical Conference and Exposition*, 1B. (2014)

Heshmat, Hooshang, James F. Walton, Brian D. Nicholson. "Ultra-High Temperature Compliant Foil Bearings – The Journey to 870°C and Application in Gas Turbine Engines: Experiment." To appear in *ASME Turbo Expo 2018: Turbine Technical Conference and Exposition*. (2018).

Carlson, M. D., A. K. Kruizenga, C. Schalansky, D. F. Fleming. "SANDIA Progress on Advanced Heat Exchangers for SCO2 Brayton Cycles." 4th International Symposium - Supercritical CO2 Power Cycles. (2014)

## ACKNOWLEDGMENTS

This material is based upon work supported by the U. S. Department of Energy under Award No. DE-SC0015811. The authors particularly acknowledge the support of Mr. Brian K. Robinson at DOE. We also acknowledge the contributions of our esteemed colleagues Andrew Hunsberger and Luke Montesano at MITI (http://www.mohawkinnovative.com) for their contributions to the development of this work.